Investigation of the Two-Dimensional Non-Hermitian Su–Schrieffer–Heeger Model

U.P. Tyagi and P. Goswami*

Physics Department, D.B. College (University of Delhi), Kalkaji, New Delhi 110019, India

Received: 07.02.2025 & Accepted: 16.07.2025

Doi: 10.12693/APhysPolA.148.40 *e-mail: physicsgoswami@gmail.com

This article presents an examination of a two-dimensional, non-Hermitian Su–Schrieffer–Heeger model, which differs from its conventional Hermitian counterpart by incorporating gain and/or loss terms, mathematically represented by imaginary on-site potentials. The time-reversal symmetry is disrupted due to these on-site potentials. Exceptional points in a non-Hermitian system feature eigenvalue coalescence and non-trivial eigenvector degeneracies. Utilization of the rank-nullity theorem and graphical analysis of the phase rigidity factor enables identification of true exceptional points. Furthermore, this investigation achieves vectorized Zak phase quantization and examines a topolectric resistors–inductors–capacitors circuit to derive the corresponding topological boundary resonance condition and the quantum Hall susceptance. Although Chern number quantization is not feasible, staggered hopping amplitudes corresponding to unit-cell lattice sites lead to broken inversion symmetry with non-zero Berry curvature, resulting in finite anomalous Nernst conductivity.

topics: Su–Schrieffer–Heeger (SSH) model, imaginary on-site potential, vectorized Zak phase, topolectric resistors–inductors–capacitors (RLC) circuit

1. Introduction

The two-dimensional (2D) non-Hermitian Su–Schrieffer–Heeger (SSH) model Hamiltonian [1, 2], representing a generalized form of the one-dimensional (1D) standard Hermitian SSH model [3–5], is used to describe topological phases in systems exhibiting non-Hermitian dynamics. To investigate a 2D model, which is the aim of this paper, it is essential to mention a few fundamental facts related to the 1D Hermitian model first [3] and then examine the effects of incorporating an additional dimension and non-Hermitian terms. The 1D model was initially developed to describe the electronic properties of polyacetylene, a conjugated polymer chain with two different sublattices. The different sublattices A and B involve the hopping parameters v and w between them. The reciprocal-space Hamiltonian matrix corresponding to the Hermitian version of 1D may be represented as $H_{\rm SSH}(k)=v+w\cos(a\,k)\sigma_x-w\sin(a\,k)\sigma_y$, where v (and w) is the intracell (and intercell) hopping amplitude, a is the lattice constant, and σ_j's are Pauli matrices acting on the sublattice (A/B) degree of freedom. The system is topologically non-trivial for $v < w$, exhibiting edge states, and it is trivial for $v > w$, exhibiting no such features. As long as the hopping amplitudes are staggered ($v \neq w$), there is an energy gap separating the lower, filled band, from the upper, empty band. However, when $v = w$, the energy gap closes at $k = \pi/a$ and the SSH model describes a conductor. A key fact in this context is the presence of topological edge states when the system is in a topologically non-trivial phase. In contrast, the non-Hermitian one-dimensional SSH models [4, 5] lead to phenomena such as complex energy spectra, dissipation, and exceptional points (EPs) [6–12].

This paper examines a non-Hermitian two-dimensional Su–Schrieffer–Heeger (2D SSH) model, which differs from its Hermitian counterpart by incorporating gain and/or loss terms that disrupt time-reversal symmetry (TRS). The parity–time symmetry (PTS) and the particle–hole symmetry (PHS), however, remain unbroken under certain conditions (see Sect. 2). In this paper, $\hat{T}$ will denote the time operator, while $\widehat{PT}$ is the parity–time operator. In Fig. 1a, a pictorial representation of this 2D model has been shown. Here, A, B, C, and D correspond to unit-cell sites of the model (square) lattice with lattice constant a. While the symbols u and t_1 stand for the hopping parameters along the x-direction (horizontal), the symbols v and t_2 are those along the y-direction (vertical). The formulation of this

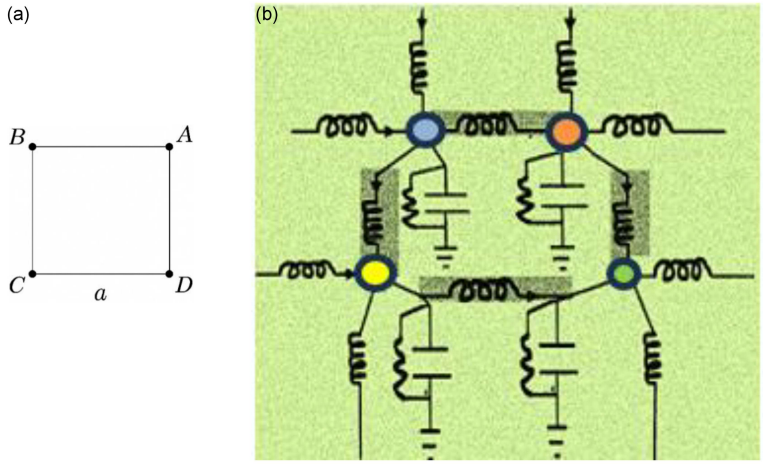

Fig. 1. A pictorial representation of a two-dimensional square lattice (lattice constant a) with unit-cell sites A, B, C, and D, arranged clockwise from the upper right corner. The hopping parameters are: u (and t_1) along the horizontal x-direction connecting A–B (and C–D) and v (t_2) along the vertical y-direction connecting B–C (and D–A). Imaginary staggered potentials are applied as: $(\mathrm{i}\gamma, -\mathrm{i}\gamma)$ to sites A and B, and $(-\mathrm{i}\gamma, \mathrm{i}\gamma)$ to sites C and D. (b) A topolectric RLC circuit with four-node represented by blue (B), red (R), green (G), and yellow (Y) nodes, corresponds to voltages V_1, V_2, V_3, and V_4, respectively. Inductors L_2 are mounted on dark bases; all others are L_1. Resistors R are connected in parallel with capacitors C. Currents I_1 and I_2, respectively, are fed into nodes B and Y from the left, while I_3 and I_4 enter nodes B and R from the top. Currents I_5 and I_6 flow through the top and bottom horizontal arms, respectively, and I_7 and I_8 flow through the left and right vertical arms.

Hamiltonian is given by $H_{\mathrm{NH,2D}}$ in real space. The imaginary staggered potentials (ISPs) are to be introduced as supplementary terms in the reciprocal space representation (see Sect. 2 for details). Such potentials, representing non-Hermitian strengths within the unit cell, are assigned values $(\mathrm{i}\gamma, -\mathrm{i}\gamma)$ and $(\mathrm{i}\gamma, -\mathrm{i}\gamma)$ for (A, B) and (C, D), respectively. The reason for their inclusion is that gain/loss may not be insignificant in real systems. We choose the wavenumber $\boldsymbol{k} = (k_x, k_y)$ to assume the values within the first Brillouin zone (BZ) in the Hamiltonian $H_{\mathrm{NH,2D}}(\boldsymbol{k})$. In Sect. 2, it will be shown that the Hamiltonian $H_{\mathrm{NH,2D}}(k_x, k_y)$ is $\widehat{PT}$-symmetric [13] if $u = t_1$. Conversely, for $u \neq t_1$, the Hamiltonian exhibits complex eigenvalues, marking the onset of a broken $\widehat{PT}$-symmetric phase. A discussion on the symmetries associated with $H_{\mathrm{NH,2D}}(k_x, k_y)$ is provided in Sect. 2.

An important aspect of the non-Hermiticity of the Hamiltonian is that it exhibits EPs [6–12], as mentioned above. In non-Hermitian Hamiltonians, exceptional points are distinguished by the merging of multiple eigenvalues and their associated eigenvectors, which often results in linear dependence among the eigenvectors. This deficiency renders the non-Hermitian Hamiltonian non-diagonalizable, bearing the algebraic signature of an exceptional point. On the other hand, the lack of conventional orthogonality among eigenvectors in the non-Hermitian realm is mitigated by employing bi-orthogonal bases. This ambiguity blurs the distinction between 'state' and 'observable', suggesting that observables no longer possess a straightforward Hermitian interpretation. To revive a probabilistic interpretation, a novel inner product is introduced, leveraging a non-trivial metric operator η (see also Sect. 5). This operator generally possesses off-diagonal elements, indicating that it introduces long-range correlations between otherwise spatially separated components, which reflects the delocalized nature of the biorthogonal basis in the non-Hermitian regime. In particular, non-Hermitian systems introduce left and right eigenvectors as a generalized form of orthogonality [14–16], where $H_{\mathrm{NH}}|u^{(j)}\rangle = E_j|u^{(j)}\rangle$ (right eigenvectors) and $H_{\mathrm{NH}}^{\dagger}|v^{(j)}\rangle = E_j^*|v^{(j)}\rangle$ or $\langle v^{(j)}|H_{\mathrm{NH}} = E_j\langle v^{(j)}|$ (left eigenvectors). Here, the eigenvalues E_j and the corresponding eigenvectors $(|u^{(j)}\rangle, \langle v^{(j)}|)$ of the Hamiltonian $H_{\mathrm{NH,2D}}(k_x, k_y)$ are indexed by $j = 1, 2, \ldots$. Moreover, these eigenvectors are not individually orthonormal in the standard sense, but collectively form a bi-orthonormal system satisfying $\langle v^{(i)}|u^{(j)}\rangle = \delta_{ij}$. The Gram matrices constructed from the right and left eigenvectors are not generally inverses of each other, i.e., $(\langle u^{(i)}|u^{(j)}\rangle \neq (\langle v^{(i)}|v^{(j)}\rangle)^{-1}$. In fact, the Gram matrices built from right/left eigenvectors can be inverses if the eigenvectors are bi-orthonormalized. Additionally, an indicator of true EPs is the phase rigidity given by the relation $P_j = |\langle v^{(j)}|u^{(j)}\rangle|/|\langle u^{(j)}|u^{(j)}\rangle|$. While a Hermitian system has $P_j = 1$ for all j when approaching

an EP, $P_j \to 0$ for the states that coalesce in a non-Hermitian system. Therefore, at EPs, one may focus on this indicator. In Sect. 2 of this paper, we report the outcome of our investigation on this issue. Furthermore, the engineering of topologically insulating and conducting phases in non-Hermitian systems is enabled by manipulating their gain and loss terms. We also show in Sect. 2 that our non-Hermitian model provides a versatile framework for creating insulating and conducting phases by controlling the interplay of gain (amplification) and loss (attenuation).

It is pertinent to mention that the Zak phase [17, 18] is a concept from topological phases of matter, typically defined for one-dimensional (1D) periodic systems, such as $H_{\rm SSH}$. It quantifies the geometric phase that arises when a wavefunction is adiabatically transported around the Brillouin zone, often used to describe systems with topological characteristics. This phase, which is a topological invariant of $H_{\rm SSH}$ — like 1D models, predicts the existence or absence of edge states in various cases [18]. The Zak phase is measured in modulo 2π. Thus, the phase is quantized to $n\pi$, where $n = 0, 1$. For our 2D system, we have obtained the vectorized Zak phase components ϕ_x and ϕ_y as a function of u/v in Sect. 3 for the tunable gain/loss parameter $\gamma = 0$ and $\gamma \neq 0$. Here, u (and v) is the hopping amplitude along the horizontal x-direction (and vertical y-direction). The results shown in Sect. 3.1 for $\gamma = 0$ indicate that the conventional bulk–boundary correspondence (BBC) depends crucially on the ratio u/v. In non-Hermitian systems ($\gamma \neq 0$), exceptional points and broken symmetries can complicate matters by causing edge modes to lose robustness or weakening the BBC. To resolve this, bi-orthonormal inner products have been employed in our analysis without disrupting the $\widehat{PT}$ symmetry. This facilitates precise predictions of edge states (see Sect. 3.2).

In this paper, we also consider a 2D resistors–inductors–capacitors (RLC) topolectric circuit [19, 20] arranged in a lattice-like structure, as shown in Fig. 1b. Here, the resistors (R), inductors (L), and capacitors (C) form a periodic structure, i.e., the one with repeating unit cells. The circuit's dynamics are governed by Kirchhoff's laws, and the admittance (or impedance) matrix — which is a function of frequency — of the circuit can describe the system's response. The equations of motion for the voltages across capacitors and the currents through inductors can be written in a matrix form, where the Hamiltonian is related to the impedance of the circuit. One needs to solve them for the eigenstates of the circuit's Hamiltonian matrix. This corresponds to finding the modes of the circuit's oscillations. The eigenstates are typically periodic wavefunctions in frequency space. The quantum Hall susceptance is calculated using the eigenfunctions corresponding to the Laplacian matrix. It is found to be positive, which indicates that the system has capacitive properties.

The quantum anomalous Hall (QAH) state is a topologically non-trivial phase characterized by an integer value of the Chern number and the presence of robust edge states that are dissipationless. The QAH effect typically occurs in systems with strong spin–orbit coupling and in the presence of a ferromagnetic order that breaks time-reversal symmetry (TRS). In a system with TRS (and inversion symmetry (IS)), the Chern number must be zero, because TRS requires that for every state at momentum $\boldsymbol{k}$, there is a time-reversed state with the opposite contribution to the Hall conductivity. The SSH model [3–5] in its standard form does not naturally support the quantum anomalous Hall state with an integer Chern number, for the standard SSH model with real hopping terms preserves TRS. However, it is possible to modify the model to include mechanisms that break TRS by introducing a magnetic field or exchange interaction. This would break TRS and induce a non-zero Chern number, leading to a topologically non-trivial phase with edge states. We shall show in Sect. 4 that the introduction of non-Hermiticity, leading to broken TRS, does not inherently create a quantum anomalous Hall effect (QAHE) with an integer Chern number. Similarly, the staggered hopping amplitudes, leading to the broken IS, do not necessarily create such a QAHE. The topological properties of the system are further highlighted by the quantum anomalous Nernst effect (QANE) — a phenomenon in which a thermoelectric current, such as the Nernst effect, is induced by an anomalous transverse thermoelectric response in a system with non-zero Berry curvature and broken IS. We will show in Sect. 4 that QANE is possible for the present system, as broken IS gives rise to a non-zero Berry curvature and non-zero, albeit non-integer, Chern number in certain parameter windows. Additionally, while QAHE is the sum of Berry curvatures of all occupied bands, QANE is computed from the Berry curvature close to the Fermi level. This implies that an insubstantial or substantial anomalous Hall effect does not necessarily imply an inconsiderable or considerable anomalous Nernst effect, due to differences in their underlying mechanisms.

The paper is organized as follows. We present the 2D SSH model in Sect. 2 and discuss its symmetry properties. We obtain the energy eigenvalues and corresponding eigenvectors in the $\widehat{PT}$-symmetric/non-symmetric cases. In Sect. 3, we calculate the Zak phase leading to the bulk–boundary correspondence. We also investigate a topolectric RLC circuit as an application of the presented model. In Sect. 4, we comment on the case where the hopping amplitudes are staggered in the $\hat{y}$-direction. The paper ends with a discussion and outlook in Sect. 5.

2. Description of the method

2.1. Model

The 2D model lattice considered here comprises sites located at $\{\boldsymbol{R}, \boldsymbol{R}+\Delta R_x\,\hat{x}, \boldsymbol{R}+2\Delta R_x\,\hat{x}, \dots\}$ in the x-direction and the same number of sites located at $\{\boldsymbol{R}, \boldsymbol{R}+\Delta R_y\,\hat{y}, \boldsymbol{R}+2\Delta R_y\,\hat{y}, \dots\}$ in the y-direction. In the absence of ISPs, the 2D model can be described by the following effective tight-binding model

$$\begin{aligned} H_{\mathrm{NH,2D}} = \sum\nolimits_R \Big(& u\,|\boldsymbol{R}, A\rangle\langle \boldsymbol{R}, B| \\ & + t_1 |\boldsymbol{R}+\Delta R_x\,\hat{x}, B\rangle\langle \boldsymbol{R}, A| + t_1 |\boldsymbol{R}, C\rangle\langle \boldsymbol{R}, D| \\ & + u\,|\boldsymbol{R}+\Delta R_x\,\hat{x}, D\rangle\langle \boldsymbol{R}, C| + v|\boldsymbol{R}, B\rangle\langle \boldsymbol{R}, C| \\ & + t_2 |\boldsymbol{R}+\Delta R_y\,\hat{y}, C\rangle\langle \boldsymbol{R}, B| + t_2 |\boldsymbol{R}, D\rangle\langle \boldsymbol{R}, A| \\ & + v|\boldsymbol{R}+\Delta R_y\,\hat{y}, A\rangle\langle \boldsymbol{R}, D|\Big) + \mathrm{h.c.} \end{aligned} \tag{1}$$

The effective tight-binding model of a crystal, in fact, is a theoretical model that describes the behavior of the crystal's vibrations in terms of the interaction between its constituent atoms or molecules. In this model, the crystal is treated as a lattice of discrete points, or 'sites,' each of which represents an atomic or molecular unit. The strength of the interaction between neighboring sites is characterized by a set of parameters, such as the hopping energies. In the present problem, these are u, v, t_1, t_2. These parameters are typically determined by fitting the model to experimental data or more detailed calculations, and can be used to obtain the energy dispersion relations.

We will now write down the Hamiltonian introduced in (1) in momentum space. As a first step, we note that the Hamiltonian in the absence of ISP may also be written slightly differently in terms of the on-site creation operator $a^\dagger_{\boldsymbol{R},1}, b^\dagger_{\boldsymbol{R},2}, \dots$ and the on-site annihilation operators $a_{\boldsymbol{R},1}, b_{\boldsymbol{R},2}, \dots$, as

$$\begin{aligned} H_{\mathrm{NH,2D}} = \sum\nolimits_{\boldsymbol{R}} \Big(& u\,a^\dagger_{\boldsymbol{R},1} b_{\boldsymbol{R},2} + u\,b^\dagger_{\boldsymbol{R},2}\,a_{\boldsymbol{R},1} \\ & + t_1\,c^\dagger_{\boldsymbol{R},3}\,d_{\boldsymbol{R},4} + t_1\,d^\dagger_{\boldsymbol{R},4}\,c_{\boldsymbol{R},3} + v\,b^\dagger_{\boldsymbol{R},2} c_{\boldsymbol{R},3} \\ & + v\,c^\dagger_{\boldsymbol{R},3}\,b_{\boldsymbol{R},2} + t_2 d^\dagger_{\boldsymbol{R},4} a_{\boldsymbol{R},1} + t_2\,a^\dagger_{\boldsymbol{R},1}\,d_{\boldsymbol{R},4} \\ & + u\,d^\dagger_{\boldsymbol{R},4} c_{\boldsymbol{R}+\Delta R_x \hat{x},3} + u\,c^\dagger_{\boldsymbol{R}+\Delta R_x\,\hat{x},3}\,d_{\boldsymbol{R},4} \\ & + v\,d^\dagger_{\boldsymbol{R}+\Delta R_y \hat{y},4}\,a_{\boldsymbol{R},1} + v\,a^\dagger_{\boldsymbol{R},1}\,d_{\boldsymbol{R}+\Delta R_y \hat{y},4} \\ & + t_1\,b^\dagger_{\boldsymbol{R}+\Delta R_x \hat{x},2}\,a_{\boldsymbol{R},1} + t_1\,a^\dagger_{\boldsymbol{R},1} b_{\boldsymbol{R}+\Delta R_x \hat{x},2} \\ & + t_2\,b^\dagger_{\boldsymbol{R},2} c_{\boldsymbol{R}+\Delta R_y \hat{y},3} + t_2\,c^\dagger_{\boldsymbol{R}+\Delta R_y \hat{y},3}\,b_{\boldsymbol{R},2}\Big). \end{aligned} \tag{2}$$

We now apply periodic boundary conditions $|\boldsymbol{R}+N\Delta\boldsymbol{R}, P\rangle = |\boldsymbol{R}, P\rangle$ in the x- and y-directions, where N is the number of sites in these directions. The Fourier transform $|R_x, P\rangle = N^{-1/2}\sum_k \mathrm{e}^{\mathrm{i}k_x R_x}|k, P\rangle$ and $|R_y, P\rangle = N^{-1/2}\sum_k \mathrm{e}^{\mathrm{i}k_y R_y}|k, P\rangle$ eventually yields

$$\begin{aligned} H_{\mathrm{NH,2D}} = & \sum\nolimits_R \sum\nolimits_k \Big\{ \Big[\frac{u}{N}|k, A\rangle\langle k, B| + \frac{t_1}{N}\mathrm{e}^{\mathrm{i}k_x(R_x+\Delta R_x)}|k, B\rangle\langle k, A|\mathrm{e}^{-\mathrm{i}k_x R_x} + \mathrm{h.c.}\Big] \\ & + \sum\nolimits_r \sum\nolimits_k \Big[\frac{t_1}{N}|k, C\rangle\langle k, D| + \frac{u}{N}\mathrm{e}^{\mathrm{i}k_x(R_x+\Delta R_x)}|k, D\rangle\langle k, C|\mathrm{e}^{-\mathrm{i}k_x R_x} + \mathrm{h.c.}\Big] \\ & + \sum\nolimits_R \sum\nolimits_k \Big[\frac{v}{N}|k, B\rangle\langle k, C| + \frac{t_2}{N}\mathrm{e}^{\mathrm{i}k_y(R_y+\Delta R_y)}|k, C\rangle\langle k, B|\mathrm{e}^{-\mathrm{i}k_y R_y} + \mathrm{h.c.}\Big] \\ & + \sum\nolimits_s \sum\nolimits_k \Big[\frac{t_2}{N}|k, D\rangle\langle k, A| + \frac{v}{N}\mathrm{e}^{\mathrm{i}k_y(R_y+\Delta R_y)}|k, A\rangle\langle k, D|\mathrm{e}^{-\mathrm{i}k_y R_y} + \mathrm{h.c.}\Big]\Big\}. \end{aligned} \tag{3}$$

We make the following replacement

$$\{|k, A\rangle, |k, B\rangle, |k, C\rangle, |k, D\rangle\} \to \{a_k, b_k, c_k, d_k\}, \tag{4}$$

where a_k, b_k, c_k, d_k are the annihilation operators in momentum space. We can then present the spinless, reciprocal space Hamiltonian in the basis $(a_k \quad b_k \quad c_k \quad d_k)^{\mathrm{T}}$ as

$$H_{\mathrm{NH,2D}}\,(k_x, k_y) = \begin{pmatrix} \varepsilon_1 & s & 0 & p \\ s^* & \varepsilon_2 & q & 0 \\ 0 & q^* & \varepsilon_1 & r \\ p^* & 0 & r^* & \varepsilon_2 \end{pmatrix}. \tag{5}$$

This reciprocal-space 2D SSH model is spinless. Therefore, the model is relevant to spin-polarized electrons and must be duplicated when applied to physical systems. Here, $\varepsilon_1 = \mathrm{i}\gamma - \mu$, $\varepsilon_2 = -\mathrm{i}\gamma - \mu$, $p = t_2 + v\exp(-\mathrm{i}ak_y)$, $s = u + t_1\exp(\mathrm{i}ak_x)$, $q = v + t_2\exp(\mathrm{i}ak_y)$, $r = t_1 + u\exp(\mathrm{i}ak_x)$, and μ is the chemical potential. The hopping parameters along the (horizontal) x- and the (vertical) y-directions are (u, t_1) and (v, t_2), respectively. The imaginary staggered potentials (ISP) on (A, B) and (C, D), respectively, are $(\mathrm{i}\gamma, -\mathrm{i}\gamma)$ and $(\mathrm{i}\gamma, -\mathrm{i}\gamma)$ and are introduced additionally to make the Hamiltonian non-Hermitian, albeit with a balanced structure. The Hamiltonian $H_{\mathrm{NH,2D}}(k_x, k_y)$ is $\widehat{PT}$-symmetric [6] if $s{=}r$ or $u{=}t_1$, i.e., $(\widehat{PT})H_{\mathrm{NH,2D}}(\widehat{PT})^{-1} = H_{\mathrm{NH,2D}}$. Here, the inversion symmetry (IS) operator is $\hat{P} = \sigma_x \otimes \sigma_x$ and the time-reversal symmetry (TRS) operator $\hat{T} = \mathbb{I}_4\,K$; $\mathbb{I}_4$ is a 4 by 4 identity matrix and K stands for complex conjugation. The inversion symmetry (IS) $(A \leftrightarrow DB \leftrightarrow C)$ requires that $H_{\mathrm{NH,2D}}(-k_x, -k_y) =$

$\hat{P}\,H_{\rm NH,2D}(k_x,k_y)\hat{P}^{-1}$, which is preserved if $u=t_1$ and $v=t_2$. We find that TRS is not preserved, i.e., $\hat{T}\,H_{\rm NH,2D}(k_x,k_y)\,\hat{T}^{-1}\neq H_{\rm NH,2D}(-k_x,-k_y)$, as the ISPs ($\pm{\rm i}\gamma$) are involved in $H_{\rm NH,2D}(k_x,k_y)$.

In particular, for $u=t_1$, one may write (5) as

$$\begin{pmatrix}\mathbb{F} & \beta\\ \beta^\dagger & \mathbb{F}\end{pmatrix},\ \text{where}\ \mathbb{F}=\begin{pmatrix}\varepsilon_1 & s\\ s^* & \varepsilon_2\end{pmatrix},\ \text{and}\ \beta=\begin{pmatrix}0 & p\\ q & 0\end{pmatrix}. \tag{6}$$

As regards chiral symmetry (the simple guess for the corresponding operator is $\hat{\Gamma}{=}\sigma_z\otimes\sigma_0$, $\hat{\Gamma}^2=\mathbb{I}\,\hat{\Gamma}^{-1}{=}\hat{\Gamma}$), we find that $H_{\rm NH,2D}$ does not anti-commute with $\hat{\Gamma}$ unless $\gamma{=}0$. We also find that if $\hat{\Gamma}$ is assumed to be $\sigma_z\otimes\sigma_0$, $\{H_{\rm NH,2D},\hat{\Gamma}\}\neq 0$ unless $r=-s$ and $p=-q^*$, which will trivialize the Hamiltonian. Thus, the Hamiltonian $H_{\rm NH,2D}$ could not be made chiral symmetric. The particle–hole symmetry ($C=\zeta K$, $\zeta=\sigma_x\otimes\sigma_z$) is satisfied by $H_{\rm NH,2D}(k_x,k_y)$, i.e., $\zeta(H^{\rm T}_{\rm NH,2D})^*$, $\zeta^{-1}=-H_{\rm NH,2D}$ if $s=r$ and $q^*=p$. This implies that $H_{\rm NH,2D}$ does not respect PHS when the horizontal bonds (s and r) in Fig. 1a do not match and the vertical bonds (q and p) (in Fig. 1a) also do not match under conjugation. Here, σ_0 and $\sigma_{x,y,z}$ are the two-by-two identity matrix and Pauli matrices, respectively. As we shall see in Sect. 4 that the broken IS ($u\neq t_1$ and $v\neq t_2$) and the broken TRS ($\gamma\neq 0$) lead to non-zero Berry curvature and the anomalous Nernst effect (ANE).

2.2. Energy eigenvalues

The energy eigenvalues of (5) are obtained by solving $\det(H_{\rm NH,2D}-\lambda\mathbb{I})=0$. The determinant leads to the quartic $Q_{A,J,\gamma}(\lambda)=\lambda^4{-}2A(k_x,k_y)\lambda^2{+}A^2(k_x,k_y){-}J(k_x,k_y)=0$, where $A=|p|^2{+}|s|^2{-}\gamma^2$, and $J=p^*(p\,s^*+q\,r)s+p(p^*s+q^*r^*)s^*$. The explicit expressions for the eigenvalues are

$$\lambda_1=\sqrt{A{+}\sqrt{J(k_x,k_y)}},\quad \lambda_2=-\sqrt{A{+}\sqrt{J(k_x,k_y)}},$$
$$\lambda_3=\sqrt{A{-}\sqrt{J(k_x,k_y)}},\quad \lambda_4=-\sqrt{A{-}\sqrt{J(k_x,k_y)}}. \tag{7}$$

The left eigenvectors (row vectors) are

$$N_j^{-1/2}\times\Big(s^*q^*r^*+p^*B_j,\quad(\lambda_j-{\rm i}\gamma)\,(p^*s+q^*r^*)\quad r^*C_j+p^*q\,s,\quad(\lambda_j-{\rm i}\gamma)\,(B_j-s^*s)\Big). \tag{8}$$

The right eigenvectors (column vectors) are

$$N_j^{-1/2}\times\Big(s\,q\,r+p\,B_j,\qquad(\lambda_j-{\rm i}\gamma)\,(p\,s^*+q\,r)\,,\qquad r\,C_j+p\,q^*s^*,\qquad(\lambda_j-{\rm i}\gamma)\,(B_j-s^*s)\Big)^{\rm T}. \tag{9}$$

Here, $B_j=\lambda_j^2+\gamma^2-q^*q$ and $C_j=\lambda_j^2+\gamma^2-s^*s$. Upon using the bi-orthogonality condition, we obtain N_j. Figure 2 presents energy eigenvalues plotted as a function of ak_x with $ak_y=0$. In Fig. 2a–b, the parameter values are $u=t_1=1$, $v=t_2=0.75$, $\mu=0$, and $\gamma=0.77$ (panel (a)) and $\gamma=0.75$ (panel (b)). However, in Fig. 2c, γ equals 0.59. Throughout this paper, we have chosen u as a unit of energy. As depicted in Fig. 2a–c, our graphical representations demonstrate that the tunable gain/loss parameter γ induces a transformation in the system from an insulator to a conductor upon decreasing its numerical value. Additionally, we observe the presence of gapless and gapped approximate Dirac cones in Fig. 2a–b [21]. Note that $H_{\rm NH,2D}$ is $\widehat{PT}$-symmetric (eigenvalues are real) if $u=t_1$ in a limited region of the two-dimensional BZ. In contrast, for $u\neq t_1$, the Hamiltonian yields complex eigenvalues, indicating a transition to a broken $\widehat{PT}$-symmetric phase. Figure 2d presents the real and imaginary parts of energy eigenvalues as a function of ak_x with $ak_y=0$, where $u\neq t_1$ (and $v\neq t_2$). The parameter values used are $u=1$, $t_1=0.8$, $v=0.75$, $t_2=0.60$, $\mu=0$, and $\gamma=0.75$. The choice corresponds to broken PTS and PHS. As shown by the solid vertical lines, the figure indicates that at momentum component values close to $ak_x=\pm 2$, both real and imaginary parts of two or more eigenvalues (and possibly the corresponding eigenvectors) of the system converge. The solid horizontal lines correspond to $\mu=0$. Furthermore, one of the conditions for exceptional points (EPs) is that the discriminant of the quartic in $Q_{A,J,\gamma}(\lambda)$ above must be zero. This condition picks out coalescing eigenvalues — a necessary condition for EPs. For the quartic $Q_{A,J,\gamma}(\lambda)=0$ with complex coefficients, one can (still) write its discriminant $\Delta(k_xk_y)=0$ for equal roots. In Fig. 2e and Fig. 2f, we have contour plotted, respectively, the real and imaginary parts of $\Delta(k_x,k_y)$ as a function of (ak_x,ak_y). The results indicate that $\Delta(k_x,k_y)\to 0$ at a large number of points in the ak_x–ak_y plane.

We are now interested in the exceptional points of $H_{\rm NH,2D}$. We notice that when $J(k_x,k_y)=0$, $Q_{A,J,\gamma}(\lambda)=Q_{A,\gamma}(\lambda)=\big(\lambda^2{-}A(k_x,k_y)\big)^2{=}0$ implies a square-root branch point structure, typical of multi-level EP physics. There are double roots at $\lambda_\pm(k_x,k_y){=}\pm\sqrt{A(k_x,k_y)}$ with algebraic multiplicity (AM) as 2. In light of (8) and (9), the eigenvector coalescence occurs

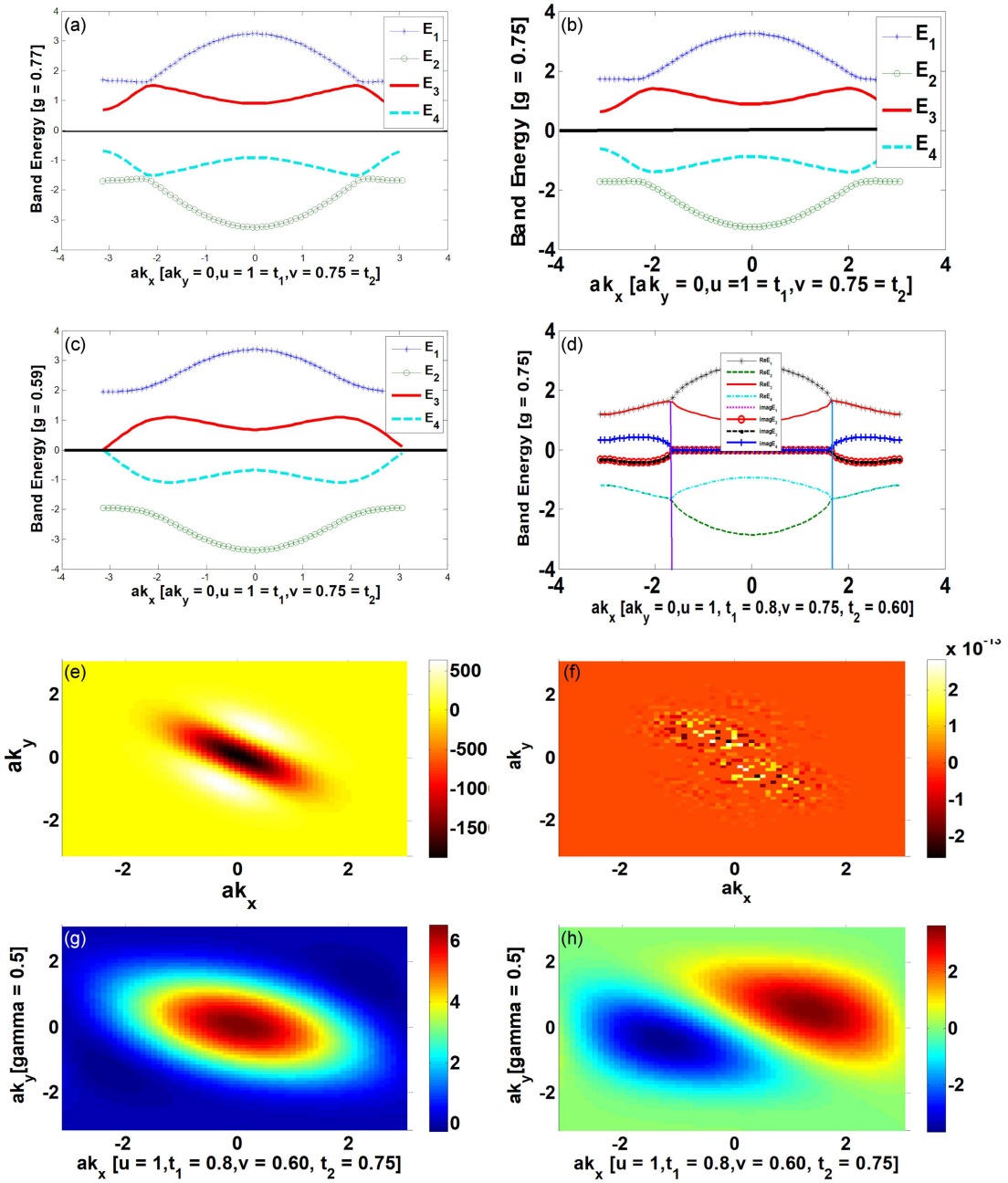

Fig. 2. (a–b) Energy eigenvalues λ_j (denoted as E_j for $j = 1, 2, 3, 4$) as a function of ak_x with $ak_y = 0$. The parameter values are $u = t_1 = 1$, $v = t_2 = 0.75$, $\mu = 0$, and $\gamma = 0.77$ (a) and $\gamma = 0.75$ (b). In panel (c), $\gamma = 0.59$. Descriptive 'gamma' means γ in our 2D SSH model. The horizontal solid line represents the Fermi energy. (d) The real and imaginary parts of the energy eigenvalues as a function of ak_x with $ak_y = 0$. The parameter values are $u = 1$, $t_1 = 0.80$, $v = 0.75$, $t_2 = 0.60$, $\mu = 0$, and $\gamma = 0.75$. The solid horizontal lines correspond to $\mu = 0$. (e) The real and (f) imaginary part of the discriminant $\Delta(k_x k_y)$ of the quartic $Q(\lambda) = 0$. (g) The real and (h) imaginary part of one of the 3×3 minors $[p^*(p\,s^* + q\,r)]$ as a function of ak_x and ak_y.

in this case. On the other hand, the geometric multiplicity (GM) of the eigenvalues is the dimension of the eigenspace corresponding to these eigenvalues, i.e., it is the number of linearly independent eigenvectors associated with $\lambda_\pm(k_x, k_y)$. Mathematically, one reads $\mathrm{GM}(\lambda_\pm) = \dim[\ker(H_{\mathrm{SSH,2D}} - \lambda_\pm \mathbb{I})]$. This is the nullity of $(H_{\mathrm{SSH,2D}} - \lambda_\pm \mathbb{I})$. By the rank-nullity theorem, nullity(matrix) = rank(matrix)+number of columns of the matrix. So, in this case, nullity = $[4 - \mathrm{rank}(H_{\mathrm{SSH,2D}} - \lambda_\pm \mathbb{I})] <$ AM of $\lambda_\pm(k_x, k_y)$ is describing the case when GM $<$ AM. To find the rank, we need to compute the determinants of all minors of $(H_{\mathrm{SSH,2D}} - \lambda \mathbb{I})$, starting from the 4×4 determinant down to the 1×1 determinant.

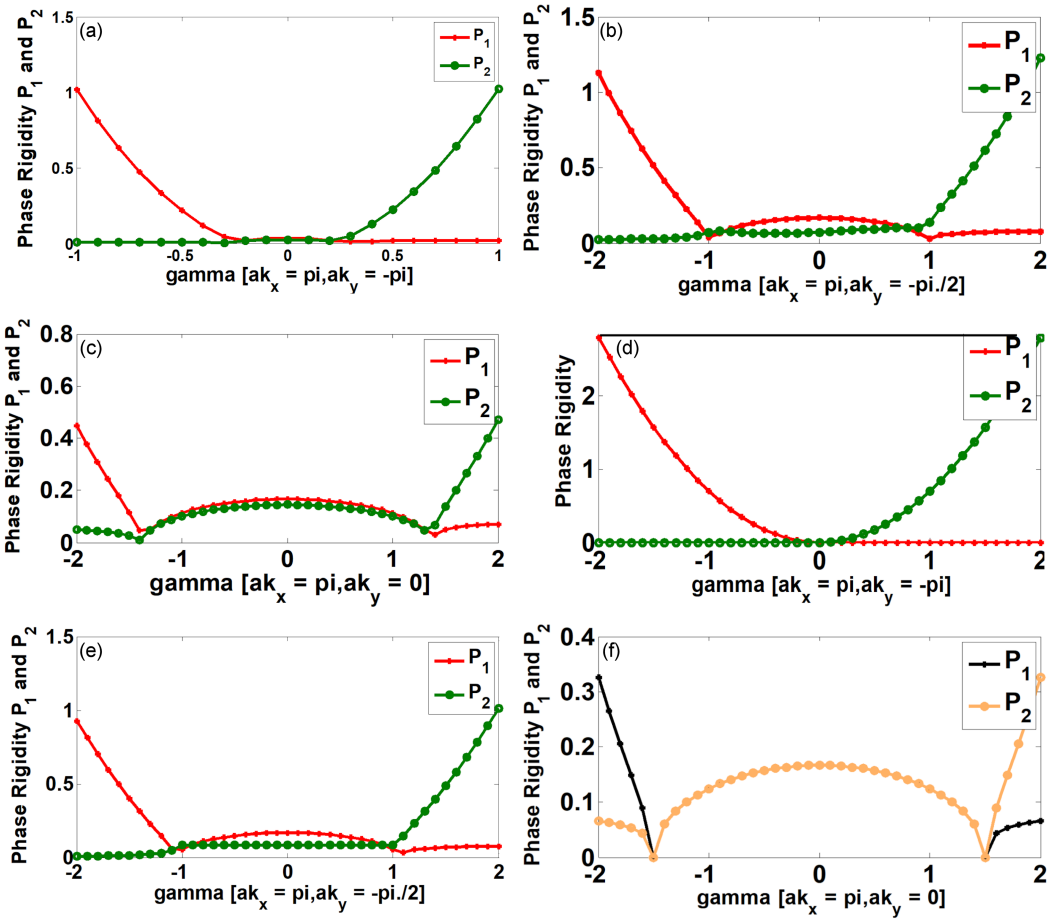

Fig. 3. (a–c) Plots of $P_1(\lambda_+)$ and $P_2(\lambda_-)$ as functions of γ for $\mu = 0$ involving staggered hopping amplitudes ($u \neq t_1$ and $v \neq t_2$). Descriptive 'gamma' means γ in our 2D SSH model. The parameter values used are $u = 1$, $t_1 = 0.80$, $v = 0.60$, and $t_2 = 0.71$. (d–f) Plots for the parameter values $u = t_1 = 1$ and $v = t_2 = 0.75$. The choice of the values leaves PTS and PHS unbroken.

If $\det(H_{\rm SSH,2D} - \lambda\,\mathbb{I}) \neq 0$, then rank $= 4$. In this case, λ is not an eigenvalue of $H_{\rm SSH,2D}$. However, if det $= 0$, we need to check all 3×3 minors. If one is non-zero, rank $= 3$. Upon going down, if all 3×3 minors vanish, one needs to check 2×2 minors. If all 2×2 minors vanish, one needs to check 1×1 entries. The largest size minor with a non-zero determinant gives the rank. In Fig. 2g and Fig. 2h, we have plotted, respectively, the real and imaginary parts of one of the 3×3 minors $[p^*(p\,s^* + q\,r)]$. The plots show the possibility of the minor being non-zero at a large number of points in the ak_x–ak_y plane. This implies that GM $= 1$, or GM $<$ AM. Thus, the Hamiltonian $H_{\rm SSH,2D}$ becomes defective (non-diagonalizable), leading to potential EPs (with AM $= 2$) at $\lambda_\pm(k_x, k_y) = \pm\sqrt{A(k_x, k_y)}$.

Next, we analyze the phase rigidity factor (PRF) $P_j = |\langle v^{(j)}|u^{(j)}\rangle|/|\langle u^{(j)}|u^{(j)}\rangle|$ graphically to identify some of the true EPs in the ak_x–ak_y plane. In Fig. 3a–c, we have plotted $P_1(\lambda_+)$ and $P_2(\lambda_-)$ as functions of γ for $\mu = 0$ involving staggered hopping amplitudes ($u \neq t_1$ and $v \neq t_2$). The parameter values used are $u = 1$, $t_1 = 0.80$, $v = 0.60$, and $t_2 = 0.71$. The choice of the parameter values breaks PTS and PHS. In Fig. 3d–f, we have plotted the same with the parameter values $u = t_1 = 1$ and $v = t_2 = 0.75$. The choice of the values leaves PTS and PHS unbroken. As we find in these panels, there are quite a few points (ak_x, ak_y) where $P_1(\lambda_+)$ and/or $P_2(\lambda_-) \to 0$. For example, $(ak_x = \pi, ak_y = -\pi)$ for $-0.3 < \gamma < +0.3$ as in Fig. 3a, $(ak_x = \pi, ak_y = -\pi/2)$ for $\gamma \sim \pm 1$ as in Fig. 3b, and $(ak_x = \pi, ak_y = 0)$ for $\gamma \simeq \pm 1.5$ as in Fig. 3c. In the PTS and PHS unbroken case, as exemplified by Fig. 3d, e, and f, one has $P_1(\lambda_+)$ and/or $P_2(\lambda_-) \to 0$ for $\gamma \sim 0$, $\gamma \sim \pm 1$, and $\gamma \sim \pm 1.5$, respectively. Thus, we find that the use of the rank-nullity theorem and the graphical analysis of the phase rigidity factor permits the identification of such points. Unique to non-Hermitian systems, these points result in enhanced sensitivity to tiny changes in system parameters (e.g., gain/loss and hopping terms) and random perturbations (e.g., weak disorder in hopping amplitudes and alteration in boundary conditions), triggering dramatically amplified responses in the system's behavior [22, 23].

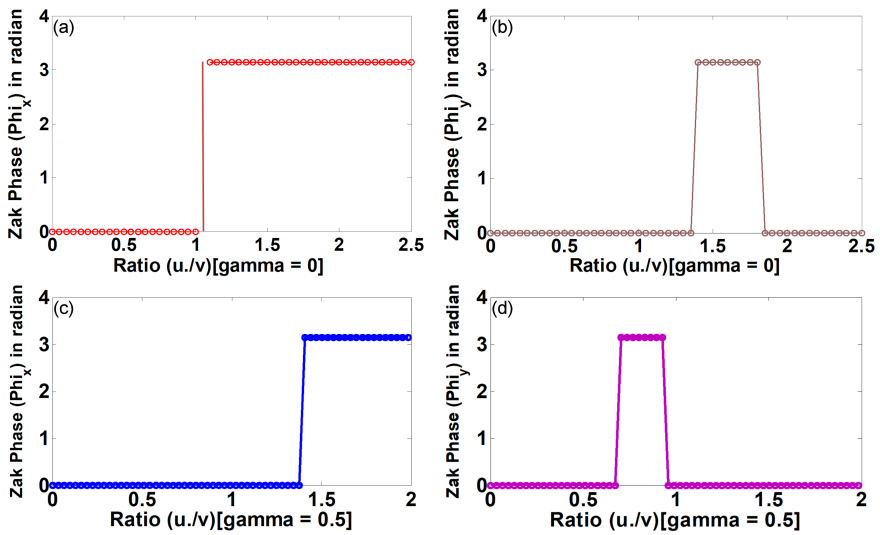

Fig. 4. Plots of the vectored Zak phase components ϕ_x and ϕ_y as a function of $\frac{u}{v}$. The choice of the hopping parameters $u = t_1$ and $v = t_2$ ensures inversion symmetry protection. We assumed (a–b) $\gamma = 0$ and (c–d) $\gamma = 0.50$.

3. Zak phase and topolectric *RLC* circuit

3.1. Zak phase

For non-Hermitian systems, the Zak phase undergoes modification due to the loss of time-reversal symmetry and the possibility of complex eigenvalues. In particular, the Zak phase for a 2D non-Hermitian SSH model represents a generalization of the 1D case (the Zak phase in 1D is essentially an integral, defined as $\phi = \oint \mathrm{d}k\, A(k)$, where $A(k)$ is the Berry connection), incorporating complex hopping terms and non-Hermitian effects like dissipation. The Zak phase in this scenario is a vector-like quantity, consisting of two components, one for each direction in the 2D system. Furthermore, non-Hermitian systems with a non-zero Zak phase may exhibit the 'non-Hermitian skin effect' [24–36], where bulk states localize at the system's boundaries due to non-Hermitian effects. In this work, by utilizing the Wilson loop approach [37, 38] and combining methodologies from references [39, 40], we have calculated the vectorized Zak phase below.

As noted above, Berry connections are essential in the context of the Zak phase. In a multi-band system, the total Berry connection cannot be expressed as a simple sum of individual Berry connections for each band, as it is contingent upon the specific wavefunctions of the bands and the inter-band couplings, which cannot be easily separated. However, if the bands are energetically well-separated and exhibit minimal inter-band coupling, the Berry connection for each band may be treated as approximately independent. We employ the parameter values close to those in Fig. 2 to calculate the Zak phase for $\gamma = 0$ and $\gamma = 0.50$. We first consider the function $\phi_x(k_y)$ for $\gamma = 0$. In this case, the Berry connection at $k_x = k_\alpha$ (where in our calculation we assumed $k_\alpha = \pi$, and $\alpha = 1, \ldots, N \gg 1$) for the j-th band is given by $A^{(j)}(k_\alpha, k_y) = \langle u^{(j)}(k_\alpha, k_y) | \mathrm{i}\partial_k | u^{(j)}(k_\alpha, k_y)\rangle$. Here, $|u^{(j)}(k_\alpha, k_y)\rangle$ is the Bloch function and j now runs over all the bands below the band gap. The Zak phase $\phi_\alpha^{(j)}(k_y)$ for the j-th Bloch band in a small segment connecting k_α and $k_{\alpha+1}$ is

$$\phi_\alpha^{(j)}(k_y) = A^{(j)}(k_\alpha, k_y)\Delta(ak_\alpha) = \mathrm{i}\langle u^{(j)}(k_\alpha, k_y) | u^{(j)}(k_{\alpha+1}, k_y)\rangle - \mathrm{i}\langle u^{(j)}(k_\alpha, k_y) | u^{(j)}(k_\alpha, k_y)\rangle. \tag{10}$$

In our numerical calculation, we have assumed $\Delta(ak_\alpha) = \Delta(ak) \ll 1$. We have used the MATLAB package for the numerical calculation. It follows that $\langle u^{(j)}(k_\alpha, k_y) | u^{(j)}(k_{\alpha+1}, k_y)\rangle = 1 - \mathrm{i}\phi_\alpha^{(j)}(k_y) \approx \exp(-\mathrm{i}\phi_\alpha^{(j)}(k_y))$. In light of the Wilson loop approach [37, 38], the total Zak phase $\phi_x(k_y)$ could be calculated by compounding the discrete Zak phase from each small segment $\Delta(ak_\alpha)$. Following [39], we find

$$\exp\left(-\mathrm{i}\phi_x\left(k_y\right)\right) = \prod_{\alpha=1}^{\alpha=N} \sum_j \left\langle u^{(j)}\left(k_\alpha, k_y\right) | u^{(j)}\left(k_{\alpha+1}, k_y\right)\right\rangle. \tag{11}$$

After using expression (11), the Zak phase component ϕ_x could be written as

$$\phi_x = \frac{1}{2\pi}\int_{-\pi}^{+\pi} \mathrm{d}k_y \ \mathrm{Im}\left\{\ln\left[\prod_{\alpha=1}^{\alpha=N}\sum_j \left\langle u^{(j)}\left(k_\alpha, k_y\right)\left|u^{(j)}\left(k_{\alpha+1}, k_y\right)\right\rangle\right]\right\}. \tag{12}$$

The other component of the vectorized Zak phase, namely ϕ_y, can be obtained in a similar manner. In non-Hermitian 2D systems ($\gamma \neq 0$), we also have the two components of the Zak phase, namely $\{\phi_x(k_y), \phi_y(k_x)\}$, defined with the help of the right and left eigenvectors ($|u^{(j)}\rangle, \langle v^{(j)}|$). We have plotted the vectorized Zak phase components ϕ_x and ϕ_y as a function of $\frac{u}{v}$ in Fig. 4a–d. The results indicate that the conventional bulk–boundary correspondence depends crucially on the ratio $\frac{u}{v}$. In Fig. 4a–b, we have assumed $\gamma = 0$, whereas in Fig. 4c–d we have assumed $\gamma = 0.50$. The hopping parameters used in panels (a)–(d) are $u = t_1$ and $v = t_2$. Furthermore, we note that ϕ_x and ϕ_y approximate $\pi = 4\arctan(1) \approx 3.1416$ (correct to 4 decimal places) with relative error $\eta = 0.0021$. The results reveal that the conventional bulk–boundary correspondence hinges significantly on the u/v ratio.

3.2. Topolectric *RLC* circuit

An *RLC* circuit arranged in a lattice-like structure, with inductors, capacitors, and resistors forming a periodic configuration, as shown in Fig. 1b, is under consideration. The relationships between voltage and current matrices in this circuit are governed by impedance, which is a function of frequency, and the energy stored in the inductors and capacitors. The equations of motion for the voltages across the capacitors and the currents through the inductors can be written in a matrix form, where the circuit Laplacian is related to the impedance of the circuit. The circuit Laplacian is utilized to describe the dynamics of the voltages in the system, typically in the form of a differential equation that governs the time evolution of the voltages across the capacitors and the currents through the inductors. The Laplacian in a topolectric circuit can be viewed as analogous to the Hamiltonian in condensed matter systems, necessitating the solution for eigenfrequencies and eigenstates of this matrix, where eigenvalues of the matrix correspond to oscillation frequencies and eigenstates describe voltage or current distributions across components. This exercise will also enable one to calculate the Zak phase, say for the topolectric circuit in Fig. 1b, to identify topological characteristics, such as protected edge states, akin to condensed matter physics. The calculation is deferred to a future article.

The preliminary investigation of the 2D topolectric circuit, presented in this section, was motivated by [19, 40–44]. We, however, begin with a simple *LC* system. It features unit cells consisting of a pair of capacitors C_1 and C_2 with identical inductors L between them and an alternating driving voltage source with frequency ω, subject to periodic boundary conditions, characterized by the grounded Laplacian of the form

$$J_{\mathrm{SSH}}(k) = \mathrm{i}\omega\left(C_1{+}C_2 - \frac{1}{\omega^2 L}\right)\sigma_0 - \mathrm{i}\omega\Big[\Big(C_1{+}C_2\cos(ak)\Big)\sigma_x + C_2\sin(ak)\sigma_y\Big]. \tag{13}$$

The σ_j's are Pauli matrices, and (ak) represents the inverse modulation wavelength. The Laplacian has a strong resemblance to the 1D SSH model. The topological boundary resonance (TBR) condition, which essentially corresponds to the secular equation of the system, gives $\omega = \sqrt{1/(LC_{eff})}$, where $C_{eff} = C_1{+}C_2 \pm \sqrt{C_1^2{+}C_2^2{+}2C_1C_2\cos(ak)}$. In what follows, we utilize the same approach to analyze the system shown in Fig. 1b.

The mapping of the current flow in a topoelectric circuits with a network of elements like resistors, inductors, and capacitors, in a form similar to a tight-binding Hamiltonians of 1D/2D SSH model, is possible [19, 40–44], where resistors (R), capacitances (C), and inductances (L) act as the hopping parameters. We consider below a topolectric *RLC* circuit, as shown in Fig. 1. The resistors (not shown) are assumed to be in parallel with the capacitors (C). Figure 1 depicts nodal points with the voltages V_1, V_2, V_3, and V_4 corresponding to the four nodes $1, 2, 3$, and 4, respectively. Upon using Kirchhoff's laws, the current flowing out of a node $j = 1, 2, 3, 4$ could be written as

$$I_{N,j} = \sum\nolimits_{k\neq j} Y_L\left(V_j - V_k\right) + Y_C V_j. \tag{14}$$

Now, (14) describes the system with the current flowing out of the node j to other nodes k, linked by admittance $Y_L = -\mathrm{i}/(\omega L)$ and the current flowing to ground with admittance $Y_C = \mathrm{i}\omega C + R^{-1}$. The driving voltage of the circuit may be assumed to have frequency ω. Upon using the formulation presented in references [19, 40], we establish below the link of topological systems, i.e., in the case of lattice systems, the indexing of eigenmodes by momentum $\boldsymbol{k}$ and band index α is possible using Bloch's theorem. Similarly, we write here for the eigenmode $\xi_{k,\alpha}(\boldsymbol{r}, \beta) = \zeta_\alpha(\boldsymbol{k}, \beta)\exp(\mathrm{i}\boldsymbol{k}\cdot\boldsymbol{r})$. Such a node (N, j) (which may be referred to as a lattice site analogous to a lattice system) is indexed by its position $\boldsymbol{r}$ and sublattice (if any) label β. The admittance between two sites $(0, \beta)$ and $(\boldsymbol{r}, \beta')$ takes the form

$$Y_{\boldsymbol{r}}^{\beta\beta'} = \left[\sum_{k,\alpha}\frac{\left|\zeta_\alpha\left(\boldsymbol{k}, \beta\right) - \zeta_\alpha\left(\boldsymbol{k}, \beta'\right)\exp\left(\mathrm{i}\boldsymbol{k}\cdot\boldsymbol{r}\right)\right|^2}{J_{k,\alpha}}\right]^{-1}. \tag{15}$$

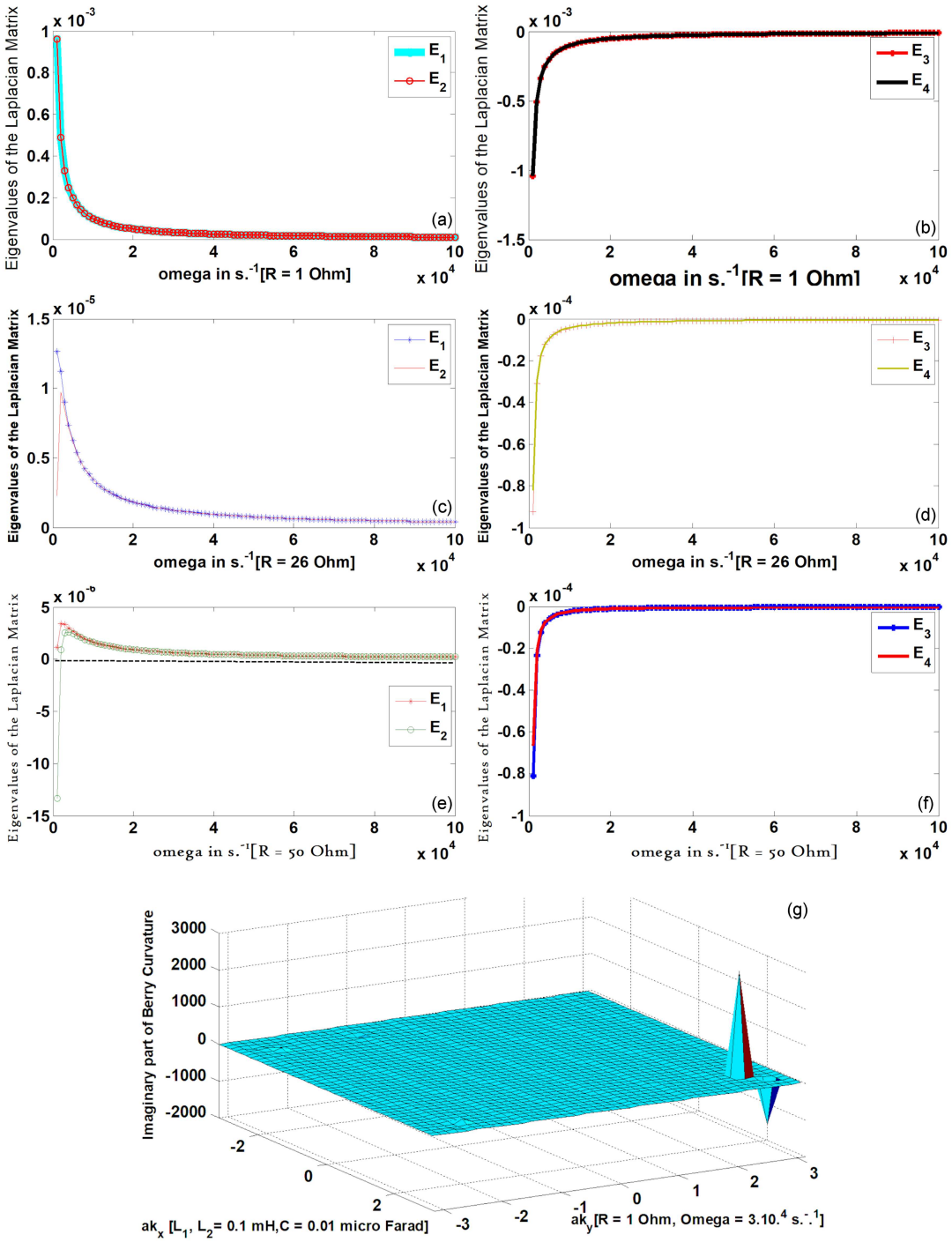

Fig. 5. (a–f) Plots of the real part E_j of eigenvalues of the circuit Laplacian matrix (19) as a function of ω in s^{-1}. The circut parameter are set as $L_1 = L_2 = 0.1$ mH and $C = 0.01$ μF. The resistance R values vary cross the panels: (a, b) 1 Ω, (c, d) 26 Ω, and (e, f) 50 Ω. (g) Plot of the imaginary component of the Berry phase for the same circuit parameters: $L_1 = L_2 = 0.1$ mH, $C = 0.01$ μF, $R = 1$ Ω, and $\omega \simeq 3 \times 10^4$ s^{-1}. This component arises from the non-Hermitian contribution to the circuit Laplacian.

The inverse wavelengths $\boldsymbol{k} = (k_x, k_y)$ take care of spatial modulation to the circuit elements in the two directions of the circuit, and $J_{k,\alpha}$ is the circuit Laplacian matrix ($\mathbb{J}$) element to be introduced into an RLC circuit. In fact, for such circuits, the voltage (V) and current (I) column vectors are related as $\mathbb{J}\boldsymbol{V} = \lambda \boldsymbol{V} = \boldsymbol{I}$. Upon comparing this fundamental circuit equations with the Schrödinger equation $H\psi = E\psi$, both in explicit matrix form, we notice that $\mathbb{J}$ has a role similar to the Hamiltonian H. Thus, if the (dimensionless) admittance between two nodes $(0, \beta)$ and $(\boldsymbol{r}, \beta')$ becomes much

less than one, there exist non-trivial eigenstates with the eigenvalues $\lambda \to 0$. This drastic increase in the impedance corresponds to the robust topological boundary resonance (TBR) condition in RLC circuits. The observation above provides us with a valuable insight that a formulation starting from circuit theory may allow us to have a sneak peek at unusual quantum phenomena.

One can write the current flowing out of the four nodes in Fig. 1b in the explicit matrix form as $\boldsymbol{I} = \mathrm{i}\omega\,\mathbb{J}\boldsymbol{V}$ with

$$\mathbb{J} = \begin{pmatrix} \mathbb{F}_1 & \zeta_1 \\ \zeta_1^\dagger & \mathbb{F}_1 \end{pmatrix}, \tag{16}$$

where

$$\mathbb{F}_1 = \begin{pmatrix} b & a_2 + a_1\exp(-\mathrm{i}k_x) \\ a_2 + a_1\exp(\mathrm{i}k_x) & b \end{pmatrix},$$

$$\zeta_1 = \begin{pmatrix} 0 & a_2 + a_1\exp(-\mathrm{i}k_y) \\ a_2 + a_1\exp(-\mathrm{i}k_y) & 0 \end{pmatrix}. \tag{17}$$

The column vectors $\boldsymbol{I}$ and $\boldsymbol{V}$ are given, respectively, as

$$\boldsymbol{I} = \begin{pmatrix} I_{N,1}\,(k_x,k_y) \\ I_{N,2}\,(k_x,k_y) \\ I_{N,3}\,(k_x,k_y) \\ I_{N,4}\,(k_x,k_y) \end{pmatrix}, \quad \text{and} \quad \boldsymbol{V} = \begin{pmatrix} V_1 \\ V_2 \\ V_3 \\ V_4 \end{pmatrix}, \tag{18}$$

and $a_1 = \frac{1}{\omega^2 L_1}$, $a_2 = \frac{1}{\omega^2 L_2}$, $b = C - \frac{\mathrm{i}}{R\omega} - 2a_1 - 2a_2$.

A comparison of (16) and (17) with (5) shows that the former has some degree of similarity to the 2D SSH model, except that a non-zero R leads to dissipation only. The eigenvalues λ_j for $j = 1,\ldots,4$ ($\mathrm{Re}(\lambda_j) = E_j(k_x,k_y)$, $\mathrm{Im}(\lambda_j)$ of the circuit Laplacian matrix given by (16) are obtained quite easily. The imaginary part of the secular equation corresponding to (16) yields $C - 2a_1 - 2a_2 = 0$. This gives $\omega = \sqrt{\frac{2}{(L_1+L_2)C}}$. For the parameter values $L_1 = L_2 = 10$ mH, and $C = 0.01$ μF, we obtain $\omega = 10^5$ s^{-1}. However, the real part of the secular equation corresponding to (16) involves the inverse modulation wavelengths (k_x, k_y). The real part yields

$$E_j\,(k_x,k_y) = C - 2a_1 - 2a_2 \pm \sqrt{\frac{1}{(R\omega)^2} + P \pm \sqrt{P^2(k_x,k_y) - Q^2(k_x,k_y)}}, \tag{19}$$

for $j = 1,2,3,4$, where

$$P\,(k_x,k_y) = 2a_1^2 + 2a_1a_2\big[\cos(k_x) + \cos(k_y)\big] + 2a_2^2, \tag{20}$$

$$Q^2\,(k_x,k_y) = \sum_{j=(x,y)} \left(2a_1^2 + 2a_1a_2\cos(k_j) + 2a_2^2\right)^2 - \Big[a_1^2 + 2a_1a_2\cos(k_y) + a_2^2\Big]\Big[2a_2^2 + 4a_1a_2\cos(k_x) + 2a_1^2\cos(2k_x)\Big]. \tag{21}$$

The plots of $E_j(k_x,k_y)$ as a function of ω for the parameter values $L_1 = L_2 = 0.1$ mH, and $C = 0.01$ μF are given in Fig. 5 for R=1 Ω (panels a–b), R=26 Ω (panels c–d), R=50 Ω (panel e–f). These plots show that the topological boundary resonance (TBR) condition $E_j = 0$ ($j = 1,2,3,4$) in the RLC circuit is satisfied when $R \simeq 1$ Ω or less. The boundary resonance occurs at $\omega \simeq 3\times10^4$ s^{-1} for all four eigenvalues obtained by equating the real(E_j) to zero. The value of the inverse wavelengths $\boldsymbol{k} = (k_x,k_y)$, which take care of spatial modulation to the circuit elements in the two directions of the circuit, has no significant influence on the value of ω. For higher resistances (as shown in Fig. 5c–f), E_j does not become zero. One may draw the conclusion that the compliance of the robust TBR condition is possible in an RLC topoelectric circuit when $R \le 1$ Ω. In other words, a larger R does not favor TBR. As noted in [40], the topological boundary resonances remain robust even in the face of significant nonuniformity of circuit elements. This promises high-precision identification in a realistic measurement. With series resistance R on the inductor, one needs to replace the impedance of each inductor, i.e., $\mathrm{i}\omega L \to \mathrm{i}\omega L + R$.

In a topolectric circuit, such as RLC circuit, the imaginary component of the Berry phase (ICBP) (ICBP$_n$ = $\int_{\mathrm{BZ}} \mathrm{d}^2k\ \mathrm{Im}[\Omega_n(k_x,k_y)]$ is relevant. This originates from the non-Hermitian (dissipative) part ($\mathrm{i}/(R\omega)$) of the RLC circuit Laplacian. The part reflects dissipation and nonconservative dynamics in the system. Upon integrating ICBP numerically or otherwise within the limits $-\pi \le (k_x,k_y) \le \pi$, we find the quantum Hall susceptance S

$$S = \sum_n \int_{-\pi}^{\pi} \mathrm{d}k_x \int_{-\pi}^{\pi} \mathrm{d}k_y\ \mathrm{Im}\left[\Omega_n(k_x,k_y)\right]. \tag{22}$$

This expression captures the net non-Hermitian topological flux through the Brillouin zone. In Fig. 5g, we have also presented a plot of the imaginary component of the Berry phase (see [45]) as a function of the inverse modulation wavelengths $\boldsymbol{k} = (k_x,k_y)$. The parameter values used in the plot are $L_1 = L_2 = 0.1$ mH, $C = 0.01$ μF, $R = 1$ Ω, and $\omega \sim 3\times10^4$ s^{-1}. Upon numerical integration (in the range $-\pi \le (k_x,k_y) \le \pi$) we find that the quantum Hall susceptance $S \simeq 0.92$ is positive, which indicates that the system has capacitive properties. It is possible to have a negative S by tuning the resistor R, in which case the system has inductive properties. The $\boldsymbol{k}$-integration process is facilitated utilizing the MATLAB package, wherein the complexity of the integration is mitigated by dividing k-space into smaller grids, enabling the integration to be performed in a manageable manner, and our approximations are refined as additional grids are incorporated. Our study in this section has successfully implemented vectorized Zak phase quantization and analyzed the topolectric

RLC circuit in Fig. 1b to determine the corresponding topological boundary resonance condition and the quantum Hall susceptance S.

4. Staggered hopping amplitudes

The presence of non-zero Berry curvature in systems with broken TRS/IS gives rise to an anomalous velocity, generally resulting in an anomalous transport current and intrinsic Hall conductivity. In this section, apart from disrupted time-reversal symmetry ($\gamma \neq 0$), we investigate a scenario where the hopping amplitudes are staggered ($u \neq t_1$, and/or $v \neq t_2$) in the horizontal and vertical ($\hat{x}$- and $\hat{y}$-) directions in Fig. 1a, causing broken IS and PHS with $\gamma = 0$. It must be emphasized that, apart from broken symmetries, an essential requirement for obtaining the integer Chern number is the existence of a band gap at $\Gamma(0,0)$ between the bands closest to the Fermi energy. If this gap does not exist, the calculation of the Chern number becomes meaningless. The $\widehat{PT}$-symmetric situation depicted in Fig. 2a and b (with $\gamma = 0.77$ and $\gamma = 0.75$, respectively) satisfies this necessary requirement under certain parameter values. In what follows, we show that the Berry curvature (BC) is finite, leading to the anomalous Nernst response (ANR) in the Hermitian system (i.e., with $\gamma = 0$), where the hopping amplitudes are staggered, and to the broken TRS system (i.e., with $\gamma \neq 0$). The finite BC emerges despite the fact that there is no spin–orbit interaction (SOI) to connect the two copies of the present Su–Schrieffer–Heeger (SSH) model describing spin-polarized electrons.

The quantum geometric tensor (QGT) [34, 46–51], denoted as $G_{\mu\nu}$, is a matrix that captures the geometry of the quantum wavefunctions in parameter space (here, momentum space $\boldsymbol{k}$). It is defined as

$$G_{n,\mu\nu}(\boldsymbol{k},\lambda) = \left\langle \frac{\partial u_{n,k}(\lambda)}{\partial k_\mu} \middle| \frac{\partial u_{n,k}(\lambda)}{\partial k_\nu} \right\rangle - \left\langle \frac{\partial u_{n,k}(\lambda)}{\partial k_\mu} \middle| u_{n,k}(\lambda) \right\rangle \left\langle u_{n,k}(\lambda) \middle| \frac{\partial u_{n,k}(\lambda)}{\partial k_\nu} \right\rangle \tag{23}$$

for a Hermitian system, where the symbol $|u_{n,k}(\lambda)\rangle$, which smoothly depends on the N-dimensional parameter $\lambda = (\lambda_1, \ldots, \lambda_N)$, stands for the n-th eigenenergy of a quantum Hamiltonian H and for a given momentum $\boldsymbol{k}$. The real part of QGT is the quantum metric tensor (QMT) $g_{n,\mu\nu}(\boldsymbol{k},\lambda)$, which defines the distance between two quantum states. Its imaginary part corresponds to the Berry curvature $\Omega_{n,\mu\nu}(\boldsymbol{k},\lambda) = -2\,\mathrm{Im}[G_{n,\mu\nu}(\boldsymbol{k},\lambda)]$. It is related to the topological properties of the system. The BC and QMT can also be written in terms of the derivatives of the Hamiltonian [46–51]. In a non-Hermitian system, QGT may still be defined, but one has to make the left eigenstates orthonormal to the right eigenstates $\langle u^{\mathrm{L}}(\lambda)|u^{\mathrm{R}}(\lambda)\rangle = \delta_{\mathrm{R,L}}$. This biorthonormality condition is a choice of normalization and not automatic. For such systems, the BC and QMT must be modified by considering the left and the right eigenstates.

Here, we calculate below the z-component of BC, namely $\Omega_\alpha^{\mu,\nu}(k_x,k_y)$, for the α-th occupied band. It is given by the formula

$$\Omega_\alpha^{\mu,\nu}(k_x,k_y) = \mathrm{i}\sum_{\beta\neq\alpha} \frac{1}{(\lambda_\alpha(k_x,k_y)-\lambda_\beta(k_x,k_y))^2}\left[\left\langle u^{(\alpha,\mu)}(k_x,k_y)\middle|\frac{\partial H_{\mathrm{NH,2D}}(k_x,k_y)}{\partial k_x}\middle|u^{(\beta,\nu)}(k_x,k_y)\right\rangle \times \left\langle u^{(\beta,\mu)}(k_x,k_y)\middle|\frac{\partial H_{\mathrm{NH,2D}}(k_x,k_y)}{\partial k_y}\middle|u^{(\alpha,\nu)}(k_x,k_y)\right\rangle - \{x\leftrightarrow y\}\right], \tag{24}$$

where the energy eigenvalues $\lambda_\alpha(k_x,k_y)$ and $\{\mu,\nu\} = \{\mathrm{L},\mathrm{R}\}$ represent the left and right eigenstates, subject to the normalization condition mentioned in Sect. 2. Notably, each of the four Berry curvatures — left–right (LR), right–left (RL), left–left (LL), and right–right (RR) — providing a unique definition of BC, exhibits local differences, but ultimately yields the same Chern number upon integration [52]. Equation (23) is what one obtains from QGT and, for a Hermitian system, it is the same as the conventional Kubo formula [53, 54]. The outline of the derivative calculation is given in Appendix. In Fig. 6a–b, we have shown the plots of BC in the z-direction for the staggered hopping amplitudes. The numerical values of the parameters used are $u = 1$, $t_1 = 0.95$, $t_2 = 0.5$, $v = 0.23$, 0.35, $\mu = 0$, and $\gamma = 0$. With these values, though TRS is respected, the inversion symmetry gets disrupted. The band gap, between the bands closer to the Fermi energy used in the plots, is $2\sqrt{A-\sqrt{J(k_x,k_y)}}$. On the other hand, the magnitude of the gap between the occupied bands is $\sqrt{A+\sqrt{J(k_x,k_y)}}+\sqrt{A-\sqrt{J(k_x,k_y)}}$. In order to investigate the Berry-phase effect in anomalous transport, we will first consider the anomalous Nernst conductivity (ANC) $\alpha_{xy}(\mu,T)$ here, which relates to the non-quantized transverse thermoelectric response. The conductivity can be computed by integrating Berry curvature with entropy density over

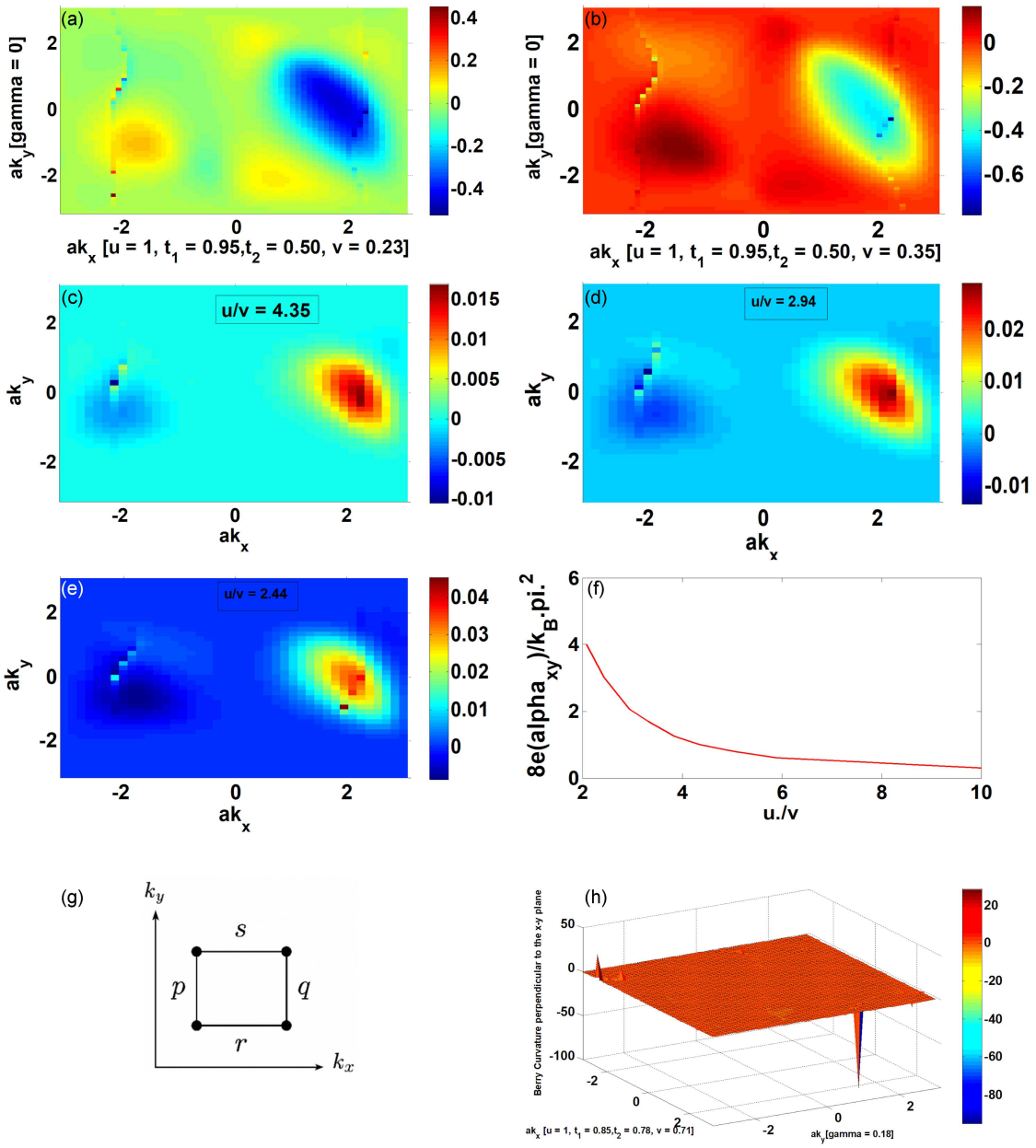

Fig. 6. (a, b) Berry curvature along the z-direction as a function of (ak_x, ak_y). The parameters used are $u = 1$, $t_1 = 0.95$, $t_2 = 0.50$, $\mu = 0$, $\gamma = 0$, $v = 0.23$ and $v = 0.35$ (respectively in (a) and (b)). (c–e) Contour plots of the integrand defined in (18). The parameters used are $u = t_1 = 1$, $t_2 = 0.5$, $\mu = 0$, and $\gamma = 0$. The values of v are 0.23, 0.34, and 0.41 in panels (c), (d), and (e), respectively. These choices ensures that inversion symmetry (IS) is broken. (f) Nernst conductivity α_{xy}, scaled by the pre-factor $3e/(\pi^2 k_B^2 T$, as a function of (u/v) at $T = 1$ K. (g) Ilustration of a path in reciprocal space showing a plaquette used in the FHS method. The figure also displays the coupling points (s, r) and (q, p). (h) Berry curvature along the z-direction obtained by the FHS method for the case of the staggered hopping amplitude. The parameters used in the plots are $u = 1$, $t_1 = 0.85$, $t_2 = 0.78$, $v = 0.71$, and $\gamma = 0.18$.

the first BZ [55, 56]. In the low-temperature limit, upon using the Mott relation [55], we obtain

$$\alpha_{xy} \approx \frac{\pi^2}{3}\frac{k_B^2 T}{e}\int \mathrm{d}\boldsymbol{k} \sum_n \Omega_{xy}^{(n)} \frac{\partial f(E_n(k))}{\partial E_n(k)}. \qquad (25)$$

Here, μ is the chemical potential, and $f(\varepsilon)$ is the Fermi–Dirac distribution. At non-zero temperatures, however, (25) becomes $\alpha_{xy}(\mu, T) = ek_B/\hbar \times \int \mathrm{d}\boldsymbol{k} \sum_n \Omega_{xy}^{(n)} s(E_n(k))$, where the entropy density is given by the expression $s(\varepsilon) = \frac{\varepsilon-\mu}{k_B T} f(\varepsilon) + \log(1+\exp(\frac{\mu-\varepsilon}{k_B T}))$; here, $f(\varepsilon) = 1/[1+\exp(\frac{\varepsilon-\mu}{k_B T})]$, where k_B — Boltzmann constant. The integrand of (25) is contour plotted in Fig. 6c–e as a function of (ak_x, ak_y) for the different values of (u/v). The numerical values of the parameters used are $u = t_1 = 1$, t_2=0.5, $\mu = 0$, and $\gamma = 0$. The

parameter v is 0.23, 0.34, and 0.41 in panels (c), (d), and (e), respectively. The choice of the values ensures broken IS. The $\boldsymbol{k}$-integration process is facilitated utilizing the MATLAB package. The Nernst conductivity α_{xy} — scaled by the pre-factors $3e/(\pi^2 k_{\rm B}^2 T)$ (in SI unit it is $\mathrm{A}^2\ \mathrm{K}\ \mathrm{s}^5/(\mathrm{kg}^2\ \mathrm{m}^5)$) — is plotted as a function of $\big(u/v\big)$ in Fig. 6f at $T = 1$ K. As one can see, as the ratio $\big(u/v\big)$ increases, the Nernst response correspondingly decreases.

The expression of the anomalous Hall conductance (AHC) is as follows

$$\sigma_{\rm AH} = \frac{e^2}{h} \sum_{\alpha\in\text{occupied bands}} \int_{\rm BZ} \frac{{\rm d}^2k}{(2\pi)^3}\, f(E_\alpha(k)-\mu)\, \Omega_\alpha^z(k), \tag{26}$$

where $f(E_\alpha(k)-\mu)$ symbolizes the fermion occupation probability of the band $E_\alpha(k)$. Whereas AHC is computed from the sum of Berry curvatures of all occupied bands, ANC is evaluated using the Berry curvature of the bands close to the Fermi level. We utilized the MATLAB package, as before, to obtain an approximate value of $\sigma_{\rm AH}$ referring to the plots of the RR-Berry curvature in the z-direction, shown in Fig. 6a and b. We obtain $\sigma_{\rm AH} \approx C(\frac{e^2}{\hbar})$, where $C = -2.3235$ in Fig. 6a ($C = -2.2290$ in Fig. 6b). We have not been able to find a suitable selection of the number of grids for which the Chern number ($C = \int_{\rm BZ} {\rm d}^2k/(2\pi)^2\, \Omega_\alpha^z(k)$) quantization is possible. We have also explored this non-quantization issue with the parameter values $u = t_1 = 1, t_2 = 0.75$, $v = 0.62$, $\mu = 0$, and $\gamma = 0.32$, 0.77, leading to TRS and IS disruption. The outcome replicated that of the earlier case. Therefore, notwithstanding the broken IS and/or TRS, anticipated to yield the possibility of the quantum anomalous Hall effect, we find that the Chern number quantization, seemingly, may not be feasible here.

To verify the non-quantization aspect of the Chern number, we have also applied the Fukui–Hatsugai–Suzuki (FHS) method [57, 58] to our model, assuming a discretized Brillouin zone. This approach leverages lattice gauge theory, employing discrete link variables instead of derivatives. The lattice boundary condition is gauge-invariant, as it is constructed from a Wilson loop or product of link variables around a plaquette, rendering it invariant under local phase redefinition of the wave functions. Figure 6g illustrates the plaquette in the reciprocal space and the couplings (s, r) and (q, p). We employed the following numerical values of the hopping parameters/ISP: $u = 1$, $t_1 = 0.85$, $t_2 = 0.78$, $v = 0.71$, $\mu = 0$, and $\gamma = 0.18$. Figure 6h displays the total BC representation across the Brillouin zone, which roughly aligns with our qualitative analysis at the high-symmetry points (HSPs). At the $\Gamma(0, 0)$ point, the couplings exhibit finite values (distinct from zero) for the chosen parameter values. The eigenvalues of ± 3.3371 and ± 0.3317, including a balanced and symmetric structure of the eigenvectors, indicate a $\widehat{PT}$-unbroken feature at this point. The symmetry between eigenvectors corresponding to $\pm$eigenvalues implies that their Berry curvatures cancel each other, resulting in zero net Berry curvature. However, individual bands retain non-zero Berry curvature.

For the other HSPs, the couplings (s, r) or/and (q, p) are close to zero, which may result in possible BC concentration at these points. At the $X(\pi, 0)$ point, there is a double eigenvalue degeneracy of both 1.4910 and -1.4910. Regarding the eigenvectors, we find there is strong symmetry and conjugation; each eigenvector has a 'partner' with mirrored real/imaginary parts and signs. Even though eigenvalues are real, the complex structure of eigenvectors obtained suggests that the curvature is likely to peak near point s, where the degeneracy is lifted. We obtain a similar feature at the $Y(0, \pi)$ point, i.e., a double degeneracy of ± 1.8460. Here, for each eigenvector, there's a partner with mirrored real and imaginary parts, and the symmetry in eigenvectors and eigenvalues suggests that Berry curvature contributions from $\pm E$ bands may cancel in total, but each band can carry non-zero curvature individually. The M point scenario, however, is different. The eigenvalue matrix is diagonal $(-0.1697, +0.1149\mathrm{i}, 0.1697, -0.1149\mathrm{i})$. The structural patterns between eigenvectors with $\pm$ imaginary eigenvalues are similar. The curvature might have imaginary components, indicating non-conservative or dissipative topological responses. The computed Chern number (C) is ≈ -2.2222. Regardless of the selection of the number of plaquettes, C results in a non-quantized value. A plausible explanation for the non-quantization is that, for non-Hermitian systems with balanced gain and loss, the corresponding curvature may not be well-behaved, leading to a breakdown in the standard definition of the Chern number.

5. Conclusions

This paper explores a 2D non-Hermitian variant of the SSH model. Our model Hamiltonian's energy eigenvalues are given by the quartic $Q_{A,J,\gamma}(\lambda) = 0$. We find that decreasing the numerical value of the tunable gain/loss parameter γ transforms the system from an insulator to a conductor. Notably, when $J = 0$, $Q_{A,\gamma}(\lambda) = 0$ leads to a square-root branch point structure typical of multi-level exceptional point (EP) physics. The utilization of the rank-nullity theorem and graphical analysis of the phase rigidity factor facilitate the identification of such points. Moreover, the Zak phase, as determined in Sect. 3.1, is an inherently geometric object unaffected by gauge selection and unit cell origin. In our 2D system with unbroken inversion symmetry, we observe that the vectorized Zak phase

components, functioning as a topological index for band characterization, display values of either 0 or π for $\gamma = 0$ and $\gamma \neq 0$ in our graphical representations in Fig. 4. The plots reveal that the conventional bulk–boundary correspondence is highly dependent on the ratio (u/v). These values indicate the existence or non-existence of gapless edge states. Importantly, the inversion symmetry-protected quantized Zak phase by itself is not quite adequate to establish the bulk–boundary correspondence, as edge states may disappear in the topological nontrivial phase, even in Hermitian systems [59–61], resulting in a breakdown of the conventional bulk–boundary correspondence. Furthermore, our analysis of the topolectric *RLC* circuit reveals that adherence to the robust topological boundary resonance (TBR) condition is attainable in the circuit when a specific condition ($R \leq 1\ \Omega$) is fulfilled; a larger value of R does not favor TBR. The quantum Hall susceptance is calculated using the eigenfunctions corresponding to the Laplacian matrix in (16), yielding a positive value indicative of capacitive properties. In Sect.4 we also examined ANC and AHC tied to a topological property of electronic wavefunctions of the model defined by (5). We found that staggered hopping amplitudes lead to broken IS with non-zero BC, resulting in finite ANC. However, we find that the Chern number quantization is not possible utilizing RR–BC. We have reconfirmed the Chern number calculation using FHS method [57, 58] for our non-Hermitian model, and our result remains unchanged. These findings represent the primary highlights of the present work.

The incorporation of asymmetric hopping or gain/loss profiles is one of the mechanisms of the origin of non-reciprocal effects in non-Hermitian systems. This asymmetry may lead to the non-Hermitian skin effect (NHSE) [62], in which bulk states migrate toward boundaries, creating edge states that dominate transport. In Hermitian systems, edge states can be predicted from bulk invariants, such as winding number. NHSE invalidates this correspondence-bulk behavior under periodic boundary condition, which will not predict the edge behavior under open boundary condition. The case in point is the 2D non-Hermitian Hatano–Nelson model [63]. One of our future goals is to explore this system using non-Bloch theory, leading to the generalized Brillouin zone (GBZ). We expect our treatment to correctly predict the presence or absence of edge states in the presence of NHSE. To explain the next goal, we pose the question, what occurs when two disparate dimensional SSH systems, each exhibiting a symmetry-protected topological phase in its respective parent dimension, are coupled together. What influence do symmetries exert in such systems? Our aim is to investigate the captivating interplay between a one-dimensional SSH and an environment characterized by the present two-dimensional SSH system, when coupled together. In general, they are expected to act as boundaries to each other, giving rise to the emergence of different dimensional gapless boundary modes in the same composite system, i.e., a zero-dimensional edge mode of the former and one-dimensional chiral boundary states hosted by the latter. Our future aim is to thoroughly investigate these two problems, with the expectation of revealing new perspectives in the study of non-Hermitian physics and the development of non-Hermitian systems.

Appendix

The right eigenstates associated with the eigenvalues of (5) can be written down in an explicit manner as $|u^{(j)}(k_x,k_y)\rangle = N_{j0}^{-1/2}\phi_j(k_x,k_y)$, where $\phi_j(k_x,k_y)$ is the transpose of the row vector $(\psi_1^{(j)}(\boldsymbol{k}),\ \psi_2^{(j)}(\boldsymbol{k}),\ \psi_3^{(j)}(\boldsymbol{k}),\ \psi_4^{(j)}(\boldsymbol{k}))$; $j{=}1,\ldots,4$, $\boldsymbol{k}{=}(k_x,k_y)$. The normalization factor N_{j0} needs to be determined using the biorthonormality condition $\langle v^{(i)}|u^{(j)}\rangle = \delta_{ij}$. The elements $\psi_\alpha^{(j)}(k)$ (with $\alpha = 1,2,3,4$) are given by

$$\begin{aligned}
\psi_1^{(j)}(k) &= \Delta_{10}^{(j)} + \mathrm{i}\Delta_{11}^{(j)},\\
\psi_2^{(j)}(k) &= \Delta_{20}^{(j)} + \mathrm{i}\Delta_{21}^{(j)},\\
\psi_3^{(j)}(k) &= \Delta_{30}^{(j)} + \mathrm{i}\Delta_{31}^{(j)},\\
\psi_4^{(j)}(k) &= \Delta_{40}^{(j)} + \mathrm{i}\Delta_{41}^{(j)}.
\end{aligned} \tag{27}$$

For the j-th band the following relations hold

$$\begin{aligned}
\Delta_{10}^{(j)} &= \Big(uvt_1 + vt_1^2\cos(ak_x)\Big) + u\,t_1t_2\cos(ak_y)\\
&\quad + t_2t_1^2\cos(ak_x{+}ak_y) + u^2v\cos(ak_x)\\
&\quad + u\,vt_1\cos(2ak_x) + t_2u^2\cos(ak_x{+}ak_y)\\
&\quad + u\,t_1t_2\cos(2ak_x{+}ak_y) - \big(t_2 + v\cos(ak_y)\big)\\
&\quad \times\big(\lambda_j^2(k){-}\gamma^2{-}|p|^2\Big),
\end{aligned} \tag{28}$$

$$\begin{aligned}
\Delta_{11}^{(j)} &= vt_1^2\sin(ak_x) + ut_1t_2\sin(ak_y)\\
&\quad + t_2t_1^2\sin(ak_x{+}ak_y) + u^2v\sin(ak_x)\\
&\quad + u\,vt_1\sin(2ak_x) + t_2u^2\sin(ak_x + ak_y)\\
&\quad + u\,t_1t_2\sin(2ak_x{+}ak_y) - v\sin(ak_y)\Big[\lambda_j^2(k){-}\gamma^2\\
&\quad -\big(v{+}t_2\exp(\mathrm{i}ak_y)\big)\big(v{+}t_2\exp(-\mathrm{i}ak_y)\big)\Big],
\end{aligned} \tag{29}$$

$$\begin{aligned}
\Delta_{20}^{(j)} &= \lambda_j(k)\Big[\big(v{+}t_2\cos(ak_y)\big)\big(t_1 + u\cos(ak_x)\big)\\
&\quad - u\,t_2\sin(ak_x)\sin(ak_y) + \big(t_2{+}v\cos(ak_y)\big)\\
&\quad \times\big(u{+}t_1\cos(ak_x)\big) - vt_1\sin(ak_x)\sin(ak_y)\Big]\\
&\quad + \gamma\Big[t_2\sin(ak_y)\big(t_1{+}u\cos(ak_x)\big) + u\sin(ak_x)\\
&\quad \times\big(v{+}t_2\cos(ak_y)\big){-}v\sin(ak_y)\big(u{+}t_1\cos(ak_x)\big)\\
&\quad -t_1\sin(ak_x)\big(t_2{+}v\cos(ak_y)\big)\Big],
\end{aligned} \tag{30}$$

$$\begin{aligned}\Delta_{21}^{(j)} &= \lambda_j(k)\Big[t_2\sin(ak_y)\big(t_1{+}u\cos(ak_x)\big)\\ &+ u\sin(ak_x)\big(v{+}t_2\sin(ak_y)\big)+v\sin(ak_y)\\ &\times\big(u{+}t_1\cos(ak_x)\big){-}t_1\sin(ak_x)\big(t_2{+}v\cos(ak_y)\big)\Big]\\ &-\gamma\Big[\big(v{+}t_2\cos(ak_y)\big)\big(t_1{+}u\cos(ak_x)\big)\\ &+u\,t_2\sin(ak_x)\sin(ak_y)+\big(t_2{+}v\cos(ak_y)\big)\\ &\times\big(u{+}t_1\cos(ak_x)\big)-vt_1\sin(ak_x)\sin(ak_y)\Big],\end{aligned} \tag{31}$$

$$\begin{aligned}\Delta_{30}^{(j)} &= |s|^2\big(v{+}t_2\cos(ak_y)\big)-\big(\lambda_j^2(k){-}\gamma^2\big)\\ &\times\big(t_1{+}u\cos(ak_x)\big)+\big(uvt_2{+}uv^2\cos(ak_y)\big)\\ &+u\,t_2^2\cos(ak_y){+}u\,v\,t_2\cos(2ak_y){+}t_1t_2v\cos(ak_x)\\ &+t_1\big(t_2^2{+}v^2\big)\cos(ak_x{+}ak_y){+}t_1t_2v\cos(2ak_y{+}ak_x),\end{aligned} \tag{32}$$

$$\begin{aligned}\Delta_{31}^{(j)} &= -|s|^2t_2\sin(ak_y)+\big(\lambda_j^2(k){-}\gamma^2\big)u\sin(ak_x)\\ &-u\,v^2\sin(ak_y)-u\,t_2^2\sin(ak_y)-uvt_2\sin(2ak_y)\\ &-t_1t_2v\sin(ak_x)-t_1(t_2^2{+}v^2)\sin(ak_x{+}ak_y)\\ &-t_1t_2v\sin(2ak_y{+}ak_x),\end{aligned} \tag{33}$$

$$\Delta_{40}^{(j)} = \lambda_j^3(k){-}\lambda_j(k)\gamma^2{-}\lambda_j(k)|p|^2{-}\lambda_j(k)|s|^2, \tag{34}$$

$$\Delta_{41}^{(j)} = \gamma^3+\gamma|p|^2+\gamma|s|^2-\gamma\lambda_j^2(k). \tag{35}$$

The quantum geometric tensor is defined in Sect. 4. The real part of the QGT is the quantum metric, and the imaginary part gives Berry curvature. Regarding the latter, using the Heisenberg equation of motion $\mathrm{i}\hbar\frac{\mathrm{d}\hat{x}}{\mathrm{d}t}=[\hat{x},\hat{H}]$, we find that the identity

$$\hbar\langle u^{(\alpha)}(k')|\hat{v_j}|u^{(\alpha)}(k)\rangle =$$

$$\big(E_\alpha(k')-E_\alpha(k)\big)\left\langle u^{(\alpha)}(k')\middle|\frac{\partial}{\partial k_j}\middle|u^{(\alpha)}(k)\right\rangle \tag{36}$$

is satisfied for a system in a periodic potential and its Bloch states as the eigenstates $|u^{(\alpha)}(k)\rangle$. Here the operator $\hbar^{-1}\frac{\partial H(k)}{\partial k_j}=\hat{v_j}$ represents the velocity in the $j=(x,y)$-direction. After applying the above identity, the z-component of BC may now be written as

$$\Omega_{xy}(k) = -2\sum_\alpha \mathrm{Im}\left[\left\langle\frac{\partial u^{(\alpha)}(k)}{\partial k_x}\middle|\frac{\partial u^{(\alpha)}(k)}{\partial k_y}\right\rangle\right]. \tag{37}$$

We use this formula to present the outline of the calculation of BC below. It is not difficult to see that for the present problem the product

$$\begin{aligned}\left\langle\frac{\partial u^{(\alpha)}(k)}{\partial k_x}\middle|\frac{\partial u^{(\alpha)}(k)}{\partial k_y}\right\rangle &= \sum_{j=1}^{4}\Big[\big(P_{jx}^{(\alpha)}P_{jy}^{(\alpha)}+Q_{jx}^{(\alpha)}Q_{jy}^{(\alpha)}\big)\\ &+\mathrm{i}\big(P_{jx}^{(\alpha)}Q_{jy}^{(\alpha)}-Q_{jx}^{(\alpha)}P_{jy}^{(\alpha)}\big)\Big],\end{aligned} \tag{38}$$

where

$$\begin{aligned}P_{jx}^{(\alpha)} &= -\frac{1}{2}N_\alpha^{-3/2}(\partial_xN_\alpha)\Delta_{j0}^{(\alpha)}+N_\alpha^{-1/2}(\partial_x\Delta_{j0}^{(\alpha)}),\\ Q_{jy}^{(\alpha)} &= -\frac{1}{2}N_\alpha^{-3/2}(\partial_yN_\alpha)\Delta_{j1}^{(\alpha)}+N_\alpha^{-1/2}(\partial_y\Delta_{j1}^{(\alpha)}),\\ Q_{jx}^{(\alpha)} &= -\frac{1}{2}N_\alpha^{-3/2}(\partial_xN_\alpha)\Delta_{j1}^{(\alpha)}+N_\alpha^{-1/2}(\partial_x\Delta_{j1}^{(\alpha)}),\\ P_{jy}^{(\alpha)} &= -\frac{1}{2}N_\alpha^{-3/2}(\partial_yN_\alpha)\Delta_{j0}^{(\alpha)}+N_\alpha^{-12}(\partial_x\Delta_{j0}^{(\alpha)}),\end{aligned} \tag{39}$$

$$(\partial_{x/y}N_\alpha) = 2\sum_{j=1}^{4}\Big[\Delta_{j0}^{(\alpha)}(\partial_{\frac{x}{y}}\Delta_{j0}^{(\alpha)})+\Delta_{j1}^{(\alpha)}(\partial_{\frac{x}{y}}\Delta_{j1}^{(\alpha)})\Big]. \tag{40}$$

The symbol ∂_x (∂_y) above stands for the differential coefficient $\frac{\partial}{\partial k_x}$ ($\frac{\partial}{\partial k_y}$). Now that we have calculated a formal expression for the BC of α band, we still need to calculate various derivatives in (24).

References

[1] S.H. Liu, W.L. Gao, Q. Zhang, S. Ma, L. Zhang, C. Liu, Y.J. Xiang, T.J. Cui, S. Zhang, *Research* **2019**, 8609875 (2019).

[2] F. Liu, *Phys. Rev. B* **108**, 245140 (2023).

[3] W.P. Su, J.R. Schrieffer, A.J. Heeger, *Phys. Rev. Lett.* **42**, 1698 (1979).

[4] P. Orlov, G.V. Shlyapnikov, D.V. Kurlov, *Phys. Rev. B* **111**, L081105 (2025).

[5] R. Nehra, D. Roy, *Phys. Rev. B* **105**, 195407 (2022).

[6] V.M. Alvarez, J. B. Vargas, L.F. Torres, *Phys. Rev. B* **97**, 121401(R) (2018).

[7] K. Kawabata, T. Bessho, M. Sato, *Phys. Rev. Lett.* **123**, 066405 (2019).

[8] C.C. Ye, W.L. Vleeshouwers, S. Heatley, V. Gritsev, C.M. Smith, *Phys. Rev. Research* **6**, 023202 (2024).

[9] Y. Ashida, Z. Gong, M. Ueda, *Adv. Phys.* **69**, 249 (2020).

[10] K. Kawabata, K. Shiozaki, M. Ueda, M. Sato, *Phys. Rev. X* **9**, 041015 (2019).

[11] J.-D. Lin, P.-C. Kuo, N. Lambert, A. Miranowicz, F. Nori, Y.-N. Chen, *Nat. Commun.* **16**, 1289 (2025).

[12] C.C. Wojcik, K. Wang, A. Dutt, J. Zhong, S. Fan, *Phys. Rev. B* **106**, L161401 (2022).

[13] A. Alase, S. Karuvade, C.M. Scandolo, *J. Phys. A Math. Theor.* **55**, 244003 (2022).

[14] J.-W. Ryu, J.-H. Han, C.-H. Yi, M.J. Park, H.C. Park, *Commun. Phys.* **7**, 109 (2024).

[15] C.M. Bender, *Rep. Prog. Phys.* **70**, 947 (2007).

[16] I. Mandal, E.J. Bergholtz, *Phys. Rev. Lett.* **127**, 186601 (2021).

[17] J. Zak, *Phys. Rev. Lett.* **62**, 2747 (1989).

[18] P. Delplace, D. Ullmo, G. Montambaux, *Phys. Rev. B* **84**, 195452 (2011).

[19] J. Dong, V. Juričić, B. Roy, *Phys. Rev. Research* **3**, 023056 (2021).

[20] T. Hoffmann, T. Helbig, F. Schindler et al., *Phys. Rev. Research* **2**, 023265 (2020).

[21] D. Geng, H. Zhou, S. Yue, Z. Sun, P. Cheng, L. Chen, S. Meng, K. Wu, B. Feng, *Nat. Commun.* **13**, 7000 (2022).

[22] C.M. Bender, *Rep. Prog. Phys.* **70**, 947 (2007).

[23] I. Mandal, E.J. Bergholtz, *Phys. Rev. Lett.* **127**, 186601 (2021).

[24] N. Okuma, K. Kawabata, K. Shiozaki, M. Sato, *Phys. Rev. Lett.* **124**, 086801 (2020).

[25] K. Kawabata, N. Okuma, M. Sato, *Phys. Rev. B* **101**, 195147 (2020).

[26] X. Zhang, T. Zhang, M.-H. Lu, Y.-F. Chen, *Adv. Phys. X* **7**, 2109431 (2022).

[27] H. Gao, H. Xue, Z. Gu, T. Liu, J. Zhu, B. Zhang, *Nat. Commun.* **12**, 1888 (2021).

[28] S. Yao, Z. Wang, *Phys. Rev. Lett.* **121**, 086803 (2018).

[29] S. Yao, F. Song, Z. Wang, *Phys. Rev. Lett.* **121**, 136802 (2018).

[30] F.K. Kunst, E. Edvardsson, J.C. Budich, E.J. Bergholtz, *Phys. Rev. Lett.* **121**, 026808 (2018).

[31] K. Yokomizo, S. Murakami, *Phys. Rev. Lett.* **123**, 066404 (2019).

[32] Y. Yi, Z. Yang, *Phys. Rev. Lett.* **125**, 186802 (2020).

[33] Z. Yang, K. Zhang, C. Fang, J. Hu, *Phys. Rev. Lett.* **125**, 226402 (2020).

[34] K. Zhang, Z. Yang, C. Fang, *Phys. Rev. Lett.* **125**, 126402 (2020).

[35] A. Ghatak, M. Brandenbourger, J. van Wezel, C. Coulais, *Proc. Natl. Acad. Sci. U.S.A.* **117**, 29561 (2020).

[36] L. Xiao, T. Deng, K. Wang, Z. Wang, W. Yi, P. Xue, *Phys. Rev. Lett.* **126**, 230402 (2021).

[37] K.G.Wilson, *Phys. Rev. D* **10**, 2445 (1974).

[38] H. Wang, X. Tang, H. Xu, J. Li, X. Qian, *npj Quantum Mater.* **7**, 61 (2022).

[39] M. Kim, J. Rho, *Nanophotonics* **9**, 3227 (2020).

[40] C.H. Lee, S. Imhof, C. Berger et al., *Commun. Phys.* **1**, 39 (2018).

[41] R.Y.Q. Xun, *Mol. Front. J.* **04**, 9 (2020).

[42] A. Blais, A.L. Grimsmo, S.M. Girvin, A. Wallraff, *Rev. Mod. Phys.* **93**, 025005 (2021).

[43] Z.B. Siu, M.B.A. Jalil et al., *Phys. Rev. B* **106**, 245128 (2022).

[44] J.C. Perez-Pedraza, J.E. Barrios-Vargas, A. Raya, arXiv:2402.05261v1 (2024).

[45] A. Fan, G.-Y. Huang, S.-D. Liang, *J. Phys. Commun.* **4**, 115006 (2020).

[46] D. Leykam, K.Y. Bliokh, C. Huang, Y.D. Chong, F. Nori, *Phys. Rev. Lett.* **118**, 040401 (2017).

[47] T. Gao, E. Estrecho, K.Y. Bliokh et al., *Nature* **526**, 554 (2015).

[48] M. Król, I. Septembre, P. Oliwa et al., *Nat. Commun.* **13**, 5340 (2022).

[49] H. Zhou, C. Peng, Y. Yoon, C.W. Hsu, K.A. Nelson, L. Fu, J.D. Joannopoulos, M. Soljačić, B. Zhen, *Science* **359**, 1012 (2018).

[50] R. Su, E. Estrecho, D. Biegańska, Y. Huang, M. Wurdack, M. Pieczarka, A.G. Truscott, T.C.H. Liew, E.A. Ostrovskaya, Q. Xiong, *Sci. Adv.* **7**, eabj8905 (2021).

[51] C.C. Ye, W.L. Vleeshouwers et al., arXiv:2305.17675 (2023).

[52] H. Shen, B. Zhen, L. Fu, *Phys. Rev. Lett.* **120**, 146402 (2018).

[53] F.D.M. Haldane, *Phys. Rev. Lett.* **93**, 206602 (2004).

[54] M. Chen, S. Wan, *J. Phys. Condens. Matter* **24**, 325502 (2012).

[55] D. Xiao, Y. Yao, Z. Fang, Q. Niu, *Phys. Rev. Lett.* **97**, 026603 (2006).

[56] D. Xiao, M.-C. Chang, Q. Niu, *Rev. Mod. Phys.* **82**, 1959 (2010).

[57] T. Fukui, Y. Hatsugai, H. Suzuki, *J. Phys. Soc. Jpn.* **74**, 1674 (2005).

[58] M. Nakamura, S. Masuda, arXiv:2401.12674v1 (2024).

[59] J.K. Asbóth, L. Oroszlány, A. Pályi, *A Short Course on Topological Insulators*, Springer, Cham 2016.

[60] T.L. Hughes, E. Prodan, B.A. Bernevig, *Phys. Rev. B* **83**, 245132 (2011).

[61] G. van Miert, C. Ortix, C.M. Smith, *2D Mater.* **4**, 015023 (2017).

[62] R. Lin, T. Tai, L. Li, C.H. Lee, *Front. Phys.* **18**, 53605 (2023).

[63] C. Hou, G. Wu, Y. Ruan, S. Chen, C.H. Lee, Z. Ni, *Phys. Rev. B* **109**, 205135 (2024).